Crashworthiness analysis of novel cactus-inspired multi-cell structures under axial crushing

Jianbo Chen[a,b], Eric Li[c*],Wenyang Liu[a,b], Yiqi Mao[a,b], Shujuan Hou[a,b*]

[a]*Department of Engineering mechanics,College of Mechanical and Vehicle Engineering, Hunan University, Changsha, 410082, China*

[b]*State Key Laboratory of Advanced Design and Manufacturing for Vehicle, Hunan University, Changsha, 410082, China*

[c]*School of School of Computing, Engineering & Digital Technologies, Teesside University, Campus Heart, Southfield Rd, Middlesbrough, UK, TS1 3BX*

Corresponding author:q.li@tees.ac.uk(E.Li); shujuanhou@hnu.edu.cn (S. Hou)

Abstract:

This study introduces an innovative cactus-inspired bionic tube (CBT) designed for enhanced energy absorption, drawing inspiration from the ribbed structure of cacti. Validation is achieved through quasi-static crushing experiments, confirming the numerical model's accuracy. Numerical simulations investigate critical factors, including structural mass, wall thickness, loading velocity, and cross-sectional configuration, revealing that optimized cross-section design can boost the specific energy absorption (SEA) of the original CBT by 15.84%. Additionally, a theoretical model is developed to forecast the mean crushing force of CBTs. Comparative analysis demonstrates the superior crashworthiness of CBTs over contemporary bionic and widely adopted multicell structures with the same mass, achieving a remarkable SEA of 11.44 J/g—exceeding maximum and minimum SEA values of these structures by 28.3% and 127.9%, respectively. This research significantly contributes to advancing the development of high-performance bionic energy-absorbing structures for crash applications.

Keywords: Crashworthiness; Multicell structures; Energy absorption; Bioinspired; Dynamic loading.

1. Introduction

Lightweight thin-walled structures (TWSs) serve as crucial energy absorbers in various engineering domains, including vehicles, aerospace, and marine engineering [1-5]. Conventional designs encompass a spectrum from circular [6–10] and triangular [11] to square [12], alongside multicell tubes [13], which have undergone extensive study and widespread application. However, the evolving crashworthiness demands for advanced vehicles have unveiled limitations in the performance of these conventional TWSs. To address this challenge, a prevalent approach involves filling empty tubes with cellular material or pressurized air to

augment the crashworthiness of thin-walled (TW) tubes. This includes the integration of foam materials [9,14–17][18–20][21], honeycomb or lattice materials [22–24][25,26], and pressurized air[27][28][29]. Notably, these filler structures often require a complex combination of two materials, and the pressurized air method necessitates intricate auxiliary equipment, rendering the facilities for this enhancement method relatively cumbersome.

In contemporary research, there is a growing trend among scholars to leverage biological structures for enhancing structural crashworthiness through bionic conceptual design. Biological structures, shaped over an extended evolutionary period, have naturally evolved to adopt optimal configurations for navigating challenging living environments. Researchers are particularly concentrating on the design of bionic energy-absorbing structures [30–35], with a specific emphasis on designs inspired by both macrostructures and microstructures found in herbaceous plants [36–38] like bamboo, horsetail, and wheat. For example, Kai et al. [39] introduced innovative bamboo-inspired tubes that showcased remarkable crashworthiness capabilities. Chen et al. [40], drawing inspiration from the intricate microstructure of bamboo, conceived bionic tubes, illustrating how bionic approaches can elevate the crashworthiness performance of conventional circular tubes. Palombini et al. [41] delved into the geometry of bamboo's vascular bundle, utilizing it as inspiration to craft bionic tubes that surpassed regular tubes in terms of energy absorption. Building on this, Hu et al. [42] pioneered the development of tubular honeycomb structures, capitalizing on the microscale attributes of bamboo. Sethi et al. [43] proposed a novel combination of bamboo and spiderweb bionic impact-resistant structures, demonstrating excellent specific energy absorption. Furthermore, common herbaceous plants such as horsetail and wheat have also emerged as valuable sources of bionic inspiration for researchers. Exploring horsetail-based bionic thin-walled tubes, Xiao et al. [44] and Yin et al. [45] engineered bionic structures with superior energy absorption capabilities. Jin et al. [46] introduced a biomimetic horsetail multicellular tube with promising applications in crash protection. Taking advantage of the unique microstructural properties of wheat, grass, and bamboo stems, Gao et al. [47] pioneered the development of bionic hierarchical hexagonal tubes with significant specific energy absorption. In a parallel effort, Ha et al. [48] emulated the cross-sectional characteristics of wheat and bamboo stems, creating bio-inspired hierarchical tubes that exhibited exceptional performance.

While the previously mentioned studies primarily focus on biomimetic analyses of common herbaceous plants like bamboo, horsetail, and wheat, it is imperative to underscore the significance of exploring biomimetic design studies of the cactus—a distinctly unique herbaceous plant. Notably, the towering upright trunk of the cactus demonstrates exceptional mechanical strength, effectively withstanding substantial wind forces and its own weight. This remarkable feat is attributed to the distinctive ribbed structure of the cactus, capitalizing on the lightweight and robust properties of both its outer surface skin and inner vascular tissues [49], as showcased in Figs.1a to 1f. Despite its potential as a rich source of inspiration for energy-absorbing structures [50], cacti have received comparatively less attention in this research domain. The biomimetic structure inspired by the cactus not only holds promise for enhanced energy absorption but also introduces a unique perspective to the field of structure design, offering novel insights and avenues for advancing biomimicry in engineering applications.

This paper presents a pioneering concept: cactus-inspired bionic tubes (CBTs). The crashworthiness of CBTs was thoroughly examined through a combination of experimental testing and numerical simulations. We explored the influence of structural mass, wall thickness, impact speed, and cross-sectional configurations on the energy absorbing characteristics of CBTs. Additionally, we developed a theoretical model for CBTs to estimate the average crushing force. The study also showcased the exceptional performance of CBTs, surpassing existing counterparts. This investigation enhances our comprehension of nature-inspired engineering and unveils innovative possibilities for applications in energy-absorbing structures through the bioinspired design principles derived from cactus structures.

2. Materials and methods

2.1 Bioinspired design

Figs 1a to 1f illustrate the distinctive morphological and anatomical features of columnar cacti [49, 51–53]. These cacti exhibit towering trunks and an upright growth pattern, primarily supported by the ribbed structure formed by the outer skin and inner vascular bundles. The ribbed structure not only imparts weight-bearing capability but also contributes to overall structural stability. The outer skin demonstrates substantial rigidity and strength, while the inner vascular tissue serves the dual purpose of transporting water and nutrients and providing

robust mechanical support to the structure [49]. Consequently, these tissues exhibit a remarkable combination of lightweight properties and strength. Drawing inspiration from the cactus's ribbed structure, we propose bionic energy-absorbing structures featuring various topological configurations, as depicted in Fig. 1b.

The present study focuses on investigating the energy absorption properties of Cactus-inspired Bionic Tubes (CBTs) with different numbers of corners (i.e., N=6, 8, 10, 12; N represents the number of corners). By employing symmetrical cross-sections, the proposed bionic structures are expected to collapse in a stable mode under axial loading.

As shown in Fig.1b, the inner and outer tubes diameters (i.e., D_i =50 mm and D_o=109 mm) are fixed. The cross-section geometry for each tube is equilateral. L_i and L_o represent the side lengths of the inner and outer tubes, respectively. L_r denotes the length of rib connecting the outer tube and inner tube. The wall thickness and the height of all CBTs is t=0.85mm and H =150mm, respectively. The other geometry parameters for each CBT are listed in Table 1.

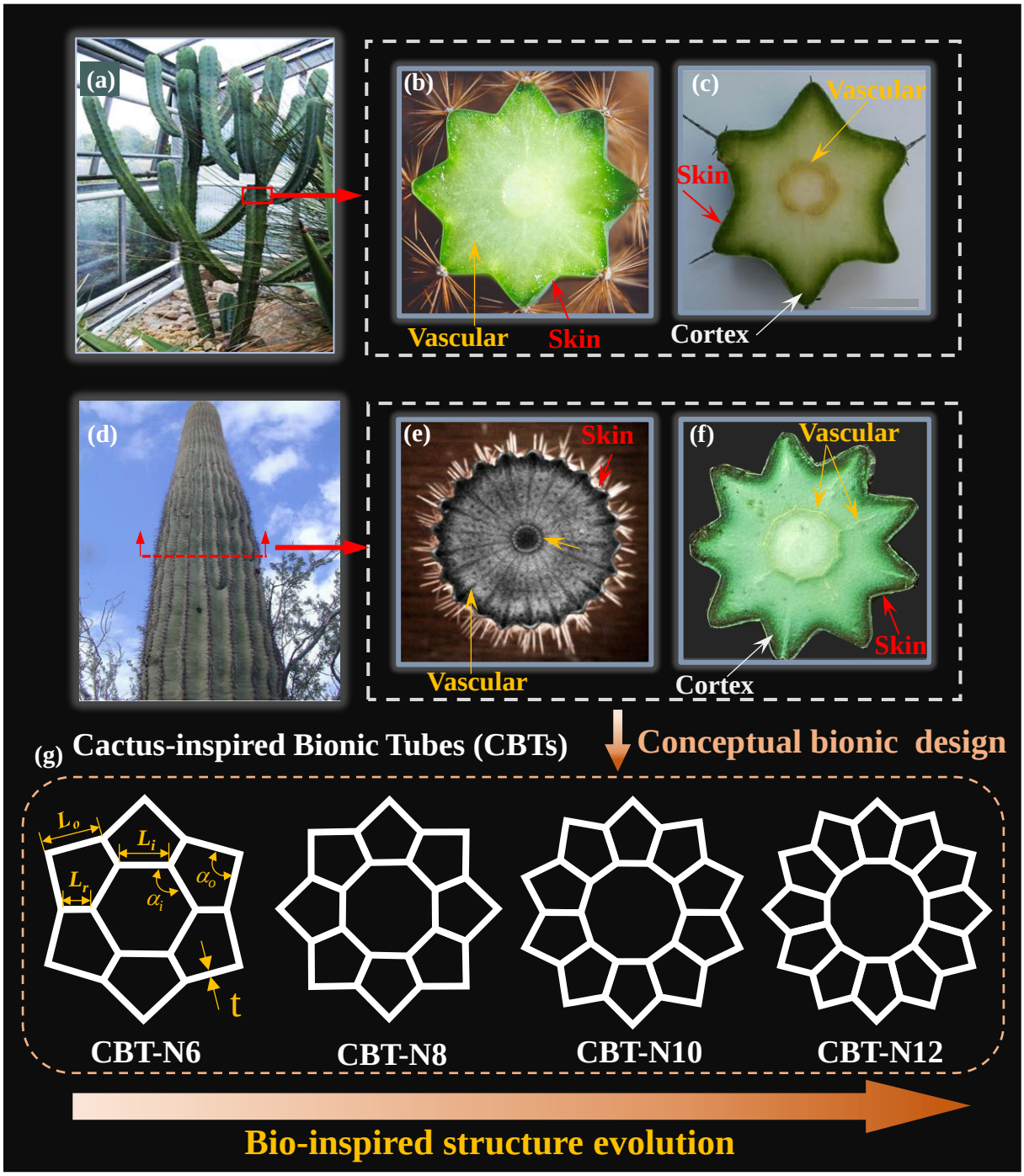

Fig.1.(a,d)The conspicuous morphologica[49,51]and (b,c,f) stem cross-sectional anatomical characteristics of columnar cacti[49,53,54]. (e)Magnetic resonance imaging image of transverse cross section for *P.mammulosa*[52]. (g) The evolution of cross section for CBTs.

Table 1 The dimension parameters of side length for CBTs.

Parameter	CBT-N6	CBT-N8	CBT-N10	CBT-N12
L_i(mm)	25	19.13	15.45	12.68
L_o(mm)	28.28	22.57	18.9	16.13
L_r(mm)	15	16.72	18.25	19.6
t(mm)	0.85	0.85	0.85	0.85

α_o	π/2	π/2	π/2	π/2
α_i	2π/3	3π/4	4π/5	5π/6

2.2 Experimental study

2.2.1 Experimental setup

The specimens of CBT were fabricated from aluminum alloy 6063-O bars by the wire-cut electrical discharge machining (WEDM) method, which has a machining accuracy of ±20μm. Only CBT-N6 was prepared as a representative specimen due to the high cost of fabrication. The fabricated specimen, which has a height of 150 mm and average thickness t of 0.85mm, is shown in Fig.2a, and its cross-sectional configuration dimension is presented in Fig.1g and Table1.

The quasi-static compression test was performed using the Instron 3382 electronic universal testing machine (load cell capability of 100kN). The schematic diagram of the crushing test setup is shown in Fig.2b. The upper platen moved downward at a speed of 0.5mm/s until the set compression displacement was reached, while the lower platen remained fixed. A camera was used to record the compression process of the specimen.

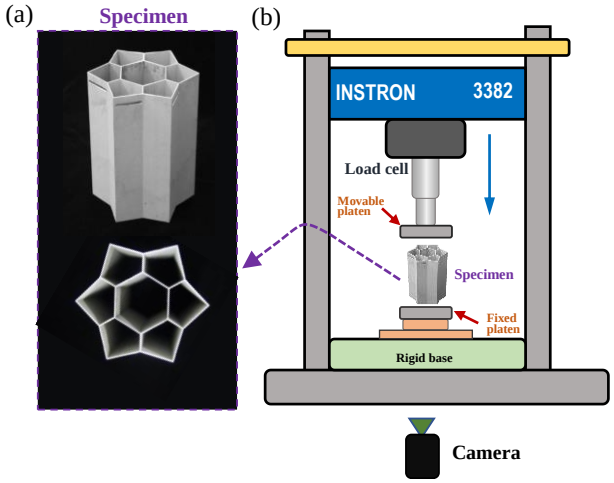

Fig.2. (a)The test specimen for CBT-N6 and (b) schematic diagram of quasi-static compression test.

2.2.2 Materials properties

Rectangular tensile samples were meticulously cut from the same aluminum alloy bar, adhering to the dimensions specified in ASTM E8/E8M-13A standards. The thickness of each tensile sample is precisely 1.5 mm, and the geometric dimensions are outlined in Fig.3. The tensile tests were conducted utilizing the Instron 3382 machine, with the crosshead speed set at 1 mm/min to maintain quasi-static loading, and the strain rate maintained at approximately 0.0004s^{-1}. To measure the strain field on the sample's surface, a 2D digital image correlation (DIC) technique was employed.The strain values were calculated using VIC 2D software (Correlated Solution Inc).

The stress-strain curve of the material is plotted in Fig.3a. The material general mechanical properties are: Young's modulus E=68.95GPa, the initial yield strength σ_y =34 MPa, the ultimate tensile strength σ_u =84 MPa, the density ρ = 2.7g/cm^3, Poisson's ratio ν =0.33. The fracture morphology of the tensile sample, captured using scanning electron microscopy (SEM) with a COXEM EM-30/X-ACT instrument, is presented in Fig.3b. The SEM image reveals the presence of numerous visible ductile dimples, indicating that the material exhibits excellent toughness. The chemical composition of the material was analyzed by energy dispersive spectroscopy (EDS) and the results are shown in Fig.3c.

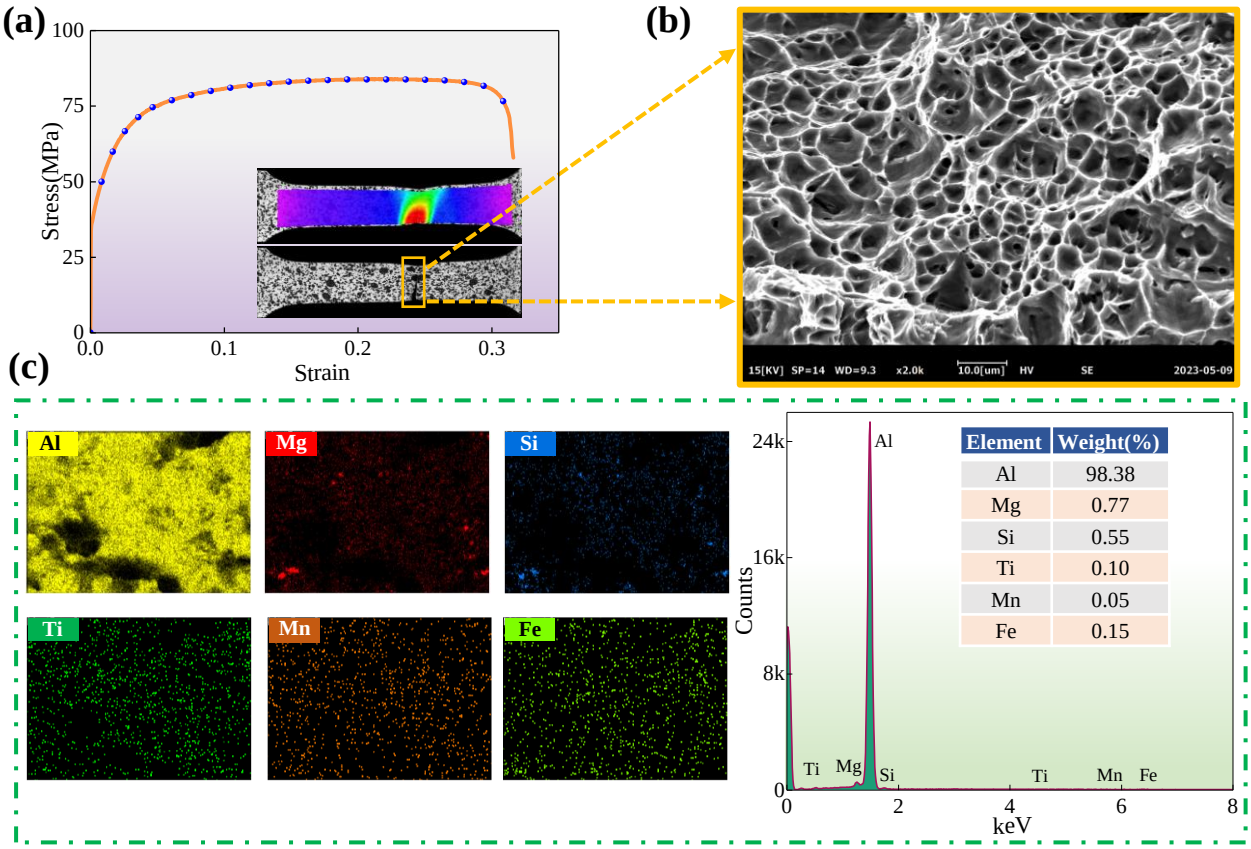

Fig.3. (a)Engineering stress-strain curve of aluminum alloy 6063-O;(b) SEM image for fracture morphology of the tensile specimen; (c) EDS mapping and spectrum for the fracture in (b).

2.3 Finite element modeling

Numerical simulations were conducted utilizing the finite element (FE) software Abaqus/explicit. Figure 4b illustrates the selection of CBT-N6 as a representative FE model positioned between two rigid platens. The CBT-N6 model was discretized using a four-node reduced integral shell element (S4R) with five integration points along the thickness direction. The rigid platen was meshed using a four-node 3D bilinear rigid quadrilateral element (R3D4). The top and bottom boundary conditions of the FE model for CBT-N6 were set as free. The upper rigid platen was movable in the axial direction, while the bottom rigid platen was fixed to support the CBT-

N6. The upper rigid platen underwent a downward displacement. A general contact algorithm was applied for all components[55], with a friction coefficient between the rigid platens and the CBT-N6 set at 0.3. The material properties of the FE model were characterized by an isotropic elastic-plastic model derived from uniaxial tensile tests in Section 2.2. Triggers with a depth of 0.3 mm were introduced below the top of the specimen based on experimental results. To achieve quasi-static results, the ratio of kinetic energy to internal energy was maintained below 5%[56]. Figure 4c depicts the mesh convergence test results, where energy absorption values for CBT-N6 were determined at a crushing distance of 100 mm. Subsequently, a mesh size of 1 mm was selected to ensure the accuracy of the numerical results.

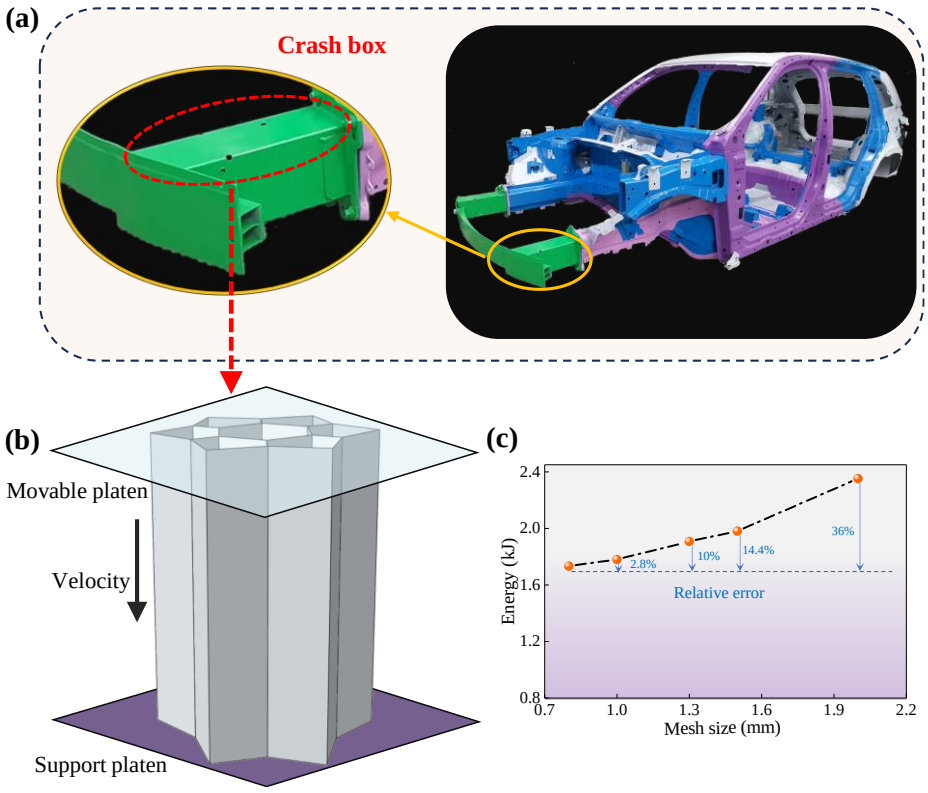

Fig.4. (a)Crash box and body structure of a car. (b)Representative FE model for CBTs under axial crushing. (c)Mesh sensitivity test on the FE model.

3 Experimental and numerical results

3.1 Numerical model validation

CBT-N6 was tested under quasi-static experiments to validate the numerical model. The deformation process of the CBT-N6 under the quasi-static test is presented in Fig.5a (Detailed crushing process and multiperspective observations of CBT-N6 are shown in Video S1, Supplementary Materials). The CBT-N6 demonstrates a sequential and consistent deformation pattern, with the first fold lobes forming in proximity

154 to the upper section of the specimen. It is found from Fig.5b that the numerical deformation mode of the
155 CBT-N6 is almost the same as the experimental observations. Both experimental and numerical results
156 indicate that CBT-N6 exhibits collapse in an asymmetrical buckling mode, with well-coordinated folded
157 deformation of adjacent corner elements. The absence of severe distortion deformation suggests that lobes do
158 not crush against each other excessively. Consequently, the CBT-N6 demonstrates stable deformation,
159 enabling sufficient plastic deformation of the material and enhancing material utilization efficiency. The final
160 deformation pattern, as depicted in Fig.6, demonstrates remarkable similarity between the numerical and
161 experimental results. Moreover, the deformation pattern exhibits graceful and regular feature, further
162 highlighting the consistent and reliable nature of the findings.

163 In addition, the numerical force response curve demonstrates a close resemblance to the experimental curve,
164 as evident in Fig.7. The minor discrepancies observed between the experimental and numerical results can
165 be attributed to errors and imperfections in the fabricated specimens, as well as the inherent complexities
166 involved in conducting experiments. Nevertheless, overall, the numerical results align well with the
167 experimental findings. Consequently, the validated high-fidelity numerical model proves capable of
168 accurately replicating the experimental observations and results under quasi-static axial crushing conditions.
169 This successful validation ensures that the numerical model can be confidently employed in subsequent
170 studies and further analysis.

171

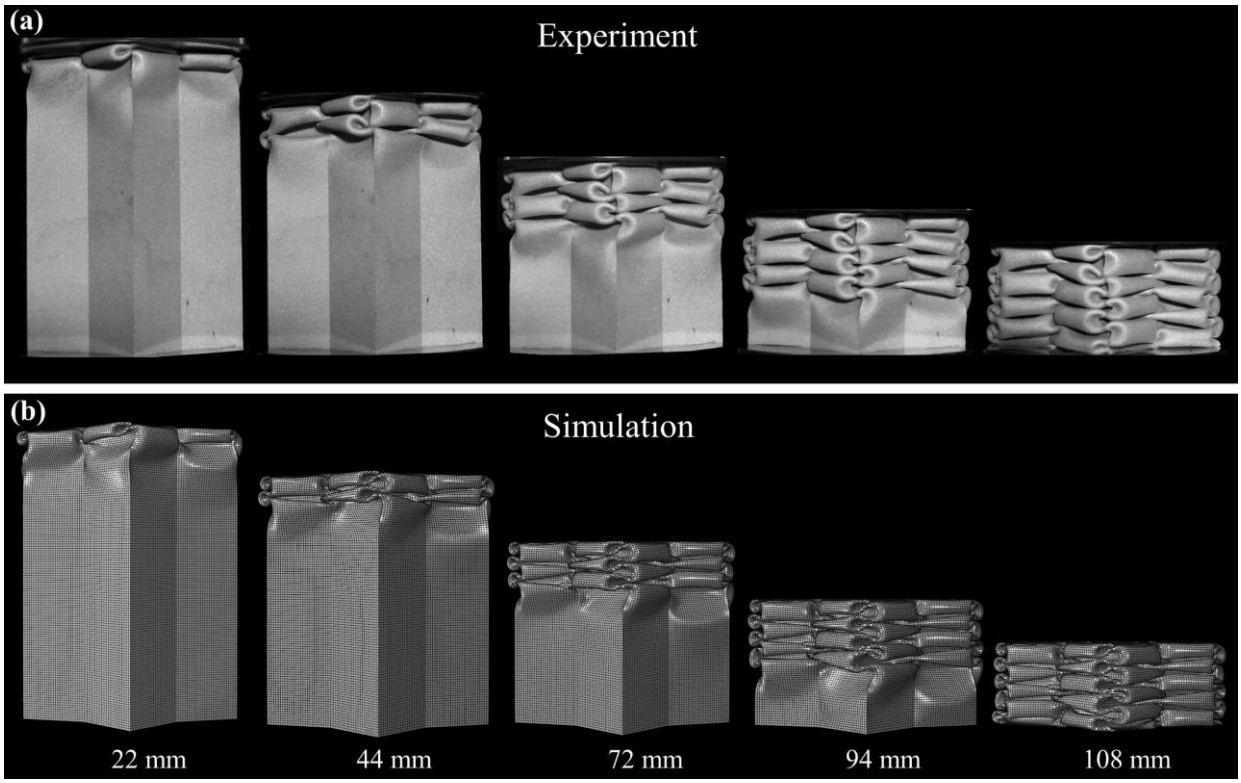

Fig.5. The axial quasi-static crushing process of CBT-N6. (a) Experimental and (b)Numerical results.

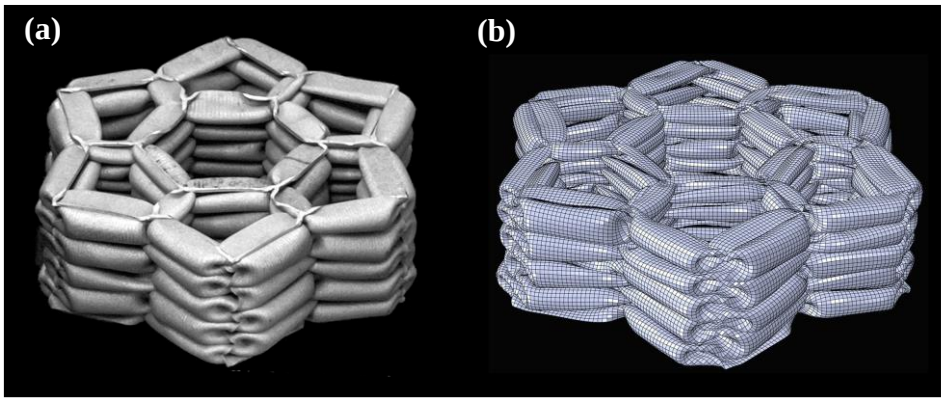

Fig.6. Comparisons of the final deformation pattern of CBT-N6 under axial quasi static load. (a)Experiment (b) FE simulation.

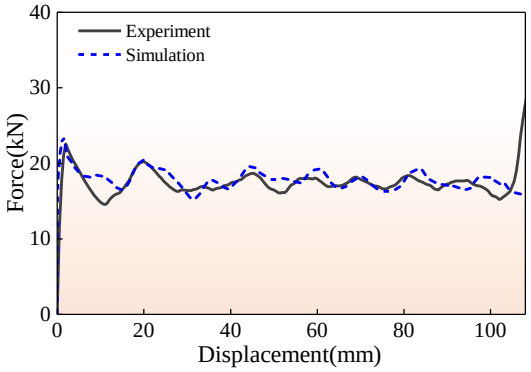

Fig.7. Force-displacement curves of CBT-N6 for the experiment and simulation under axial quasi-static load.

3.2 Deformation behaviors and force response curves of CBTs

Fig. 8 clearly shows that CBTs exhibit a stable and uniform deformation pattern, characterized by a non-extensional progressive mode of deformation. This desirable attribute contributes to effective energy absorption during the crush deformation process. On average, CBT-N6 to CBT-N12 develop approximately 4.5, 5, 6, and 6.5 regular buckling deformation layers, respectively. Regarding the folded lobes' profile, focusing on the leftmost fold as a representative, it can be observed that the number of folds increases gradually with *N*. Specifically, CBT-N6 has approximately 4 folds, CBT-N8 has 5 folds, CBT-N10 has 6 folds, and CBT-N12 has 7 folds, respectively. Notably, the number of folds of the CBTs is formed at the same crush displacement, specifically the compression distance of 114 mm. As a result, we can conclude that the half-wavelength (λ) of folding lobes decreases gradually from CBT-N6 to CBT-N12, i.e., $\lambda_4<\lambda_3<\lambda_2<\lambda_1$. Among all the CBTs, CBT-N12 exhibits the highest number of folds. Consequently, a larger proportion of the material in CBT-N12 undergoes plastic deformation, leading to improved material utilization and energy absorption efficiency of the structure.

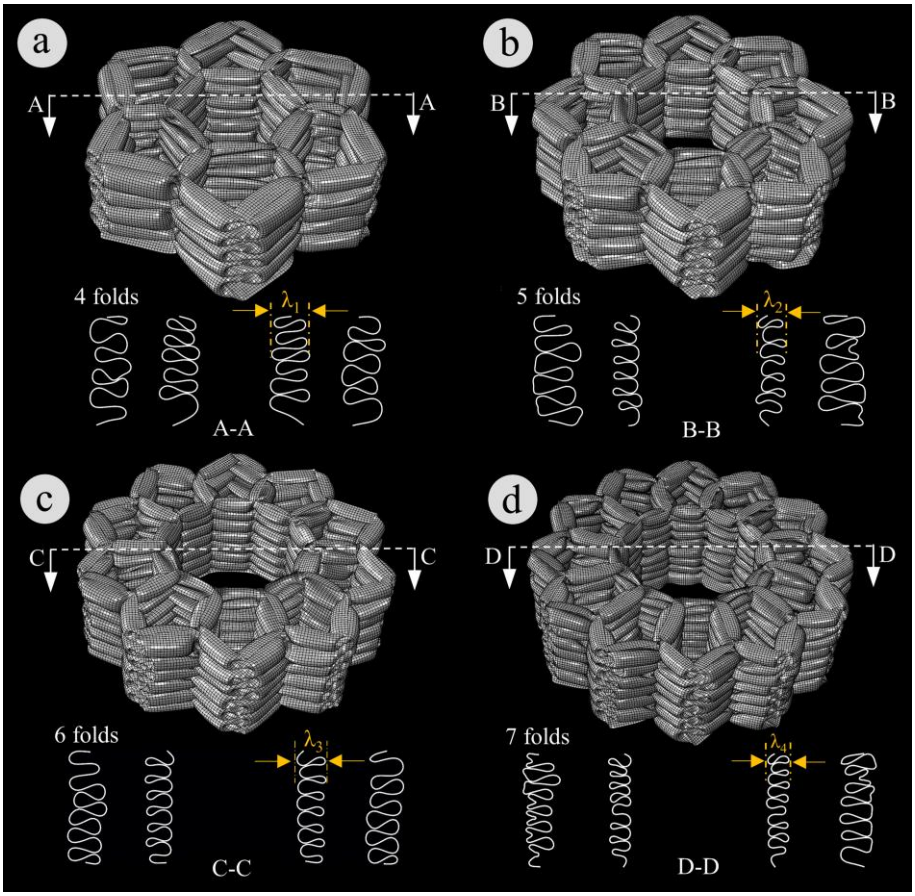

Fig.8. The simulated deformation patterns and the profiles of CBTs. (a)CBT-N6;(b) CBT-N8;(c) CBT-N10;(d) CBT-N12.

The force response curves (refer to Fig.9) reveal that during the initial crushing phase, the crushing force demonstrates a clear upward trend. After reaching its peak value, the force begins to decrease, marking the transition to the stable crushing plateau. The curve during this stage exhibits fluctuations but maintains an overall stable pattern. Subsequently, the process enters the densification stage, where the crushing force experiences a sharp increase. Furthermore, the level of the force response curve gradually rises with increasing *N*.

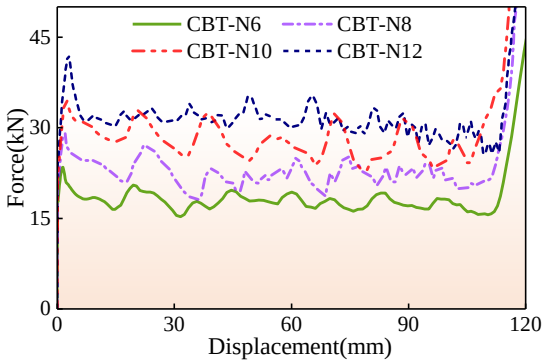

Fig.9. The force-displacement curves of the CBTs in numerical results.

3.3 Energy absorption analysis

Some key parameters have been introduced to characterize the energy absorption performance of TW structures [57,58], namely, initial peak crushing force (PCF), total energy absorption (EA),specific energy absorption (SEA),mean crushing force (MCF) , and crush force efficiency (CFE). PCF presents the maximum peak force during the initial stage of compression. EA is obtained by:

$$\mathrm{EA}=\int_0^d F(x)dx \tag{1}$$

d is the effective displacement of the compression, and *F*(*x*) denotes the instantaneous compression force. SEA is the energy absorbed per unit of mass:

$$\mathrm{SEA}=\frac{\mathrm{EA}}{m}=\frac{\int_0^d F(x)dx}{m} \tag{2}$$

where *m* is the total weight of the structure. The calculation formula for MCF is：

$$\mathrm{MCF}=\frac{\mathrm{EA}}{d}=\frac{\int_0^d F(x)dx}{d} \tag{3}$$

CFE measures the consistency of the crushing force and can be calculated by,

$$CFE = \frac{MCF}{PCF} = \frac{\int_0^d F(x)dx}{d}\frac{1}{PCF} \quad (4)$$

The important energy absorption parameters are displayed in Fig.10 and listed in Table 2. All the parameters were determined at a crush distance of d=110 mm. It is observed from Fig.10a that the PCF values are increased with N, which because the transverse cross-section of area of CBTs is increased with N, resulting in an increase in the initial stiffness of the structure. The improvement of PCF from CBT-N8 to CBT-N12 was approximately 23.9%,47.9% and 79.5% higher than that of CBT-N6, respectively.

When comparing CBT-N6 to CBT-N8, CBT-N10, and CBT-N12, it can be observed that both the MCF and EA experience an increase of 26.2%, 56 and 75.9% respectively, as shown in Fig.10a.This notable improvement can be attributed to the increase in the number of corners and ribs as N increases. The joints formed at the intersections of the ribs with the internal and external tubes, along with the corner elements, undergo a complex plastic deformation mechanism. As a result, the structure exhibits enhanced energy absorption and increased crushing force with an increase in N.

The SEA is indeed a crucial indicator when evaluating the energy absorption performance of a structure. As depicted in Fig.10b, CBT-N12 demonstrates the highest SEA among the examined CBTs, followed by CBT-N10, CBT-N8, and CBT-N6. Furthermore, it is worth noting that for N values less than or equal to 10, the CFE of the CBTs slightly increases with an increase in N (Fig.10b). However, when N reaches 12, a minor decrease in CFE is observed. This decrease can be attributed to the fact that the rate of increase in PCF surpasses the rate of increase in MCF, leading to a downward trend in CFE. Notably, the CFE of CBT-N10 is higher than that of the other CBTs, indicating a relatively stable collapse process. Overall, CBT-N12 exhibits the best performance, particularly with its highest SEA among all the tested CBTs.

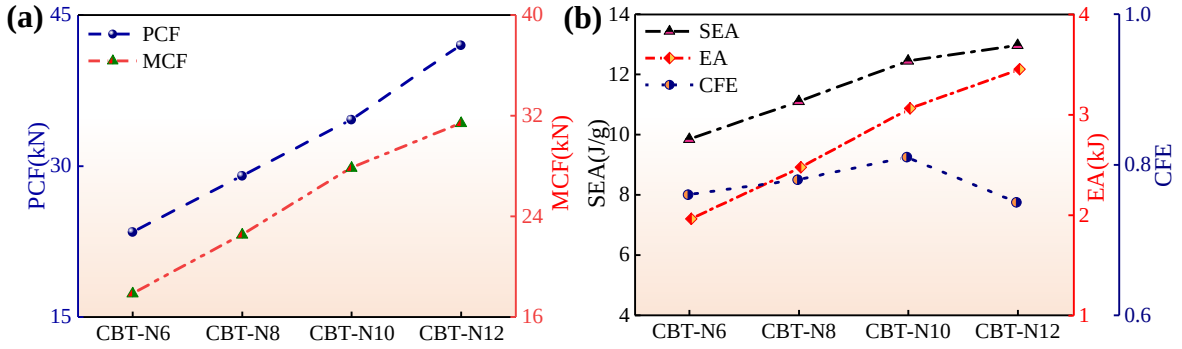

Fig.10. Energy absorption indicators of CBTs under axial quasi-static load. (a)PCF and MCF;(b) SEA, EA and CFE.

240 **Table 2** Crushing response parameters of the CBTs obtained from numerical simulations.

Specimen	Mass(g)	PCF (kN)	MCF (kN)	SEA (kJ/kg)	EA (J)	CFE
CBT-N6	199.44	23.4	17.85	9.84	1962.77	0.76
CBT-N8	223.12	29	22.52	11.10	2476.61	0.78
CBT-N10	246.14	34.6	27.84	12.44	3062.44	0.81
CBT-N12	266.61	42	31.40	12.96	3453.98	0.75

241

242 ## *4. Parametric analysis*

243 The energy absorption properties of CBTs are significantly influenced by various important factors, such
244 as the mass of the structure, wall thickness, loading velocity, and the topological configuration of the
245 structural cross-section. Hence, it is crucial and necessary to conduct a systematic study to understand the
246 impact of these factors on the energy absorption characteristics of the structures. In this analysis, we utilized
247 the validated numerical model established in Section 3.1 to further investigate these influences. For all cases
248 examined, the default bottom boundary condition of the FE model remained unfixed. Additionally, we
249 implemented the same triggers as described in Section 2.3 within the FE model to ensure consistency and
250 accuracy in our analysis.

251 ### *4.1 Effect of structural mass*

252 In this section, we conducted an analysis of the crushing behavior of CBTs with the same mass. We
253 explored four groups, where the weight of the structures within the same group was kept the same, resulting
254 in different wall thicknesses for each structure within the same group. The key parameters for each group are
255 summarized in Table3. Extensive numerical simulations were carried out and the crushing response
256 performance of the CBTs is also provided in Table 3. The findings revealed that CBTs in all groups exhibit
257 consistent inextensional deformation patterns characterized by stable and regular folding deformations. These
258 deformation patterns are well-suited for efficient energy absorption. Due to space limitations, only Group A
259 is presented in Fig.11 as a representative example, showcasing the deformation shape of the specimen at the
260 densification crushing stage.

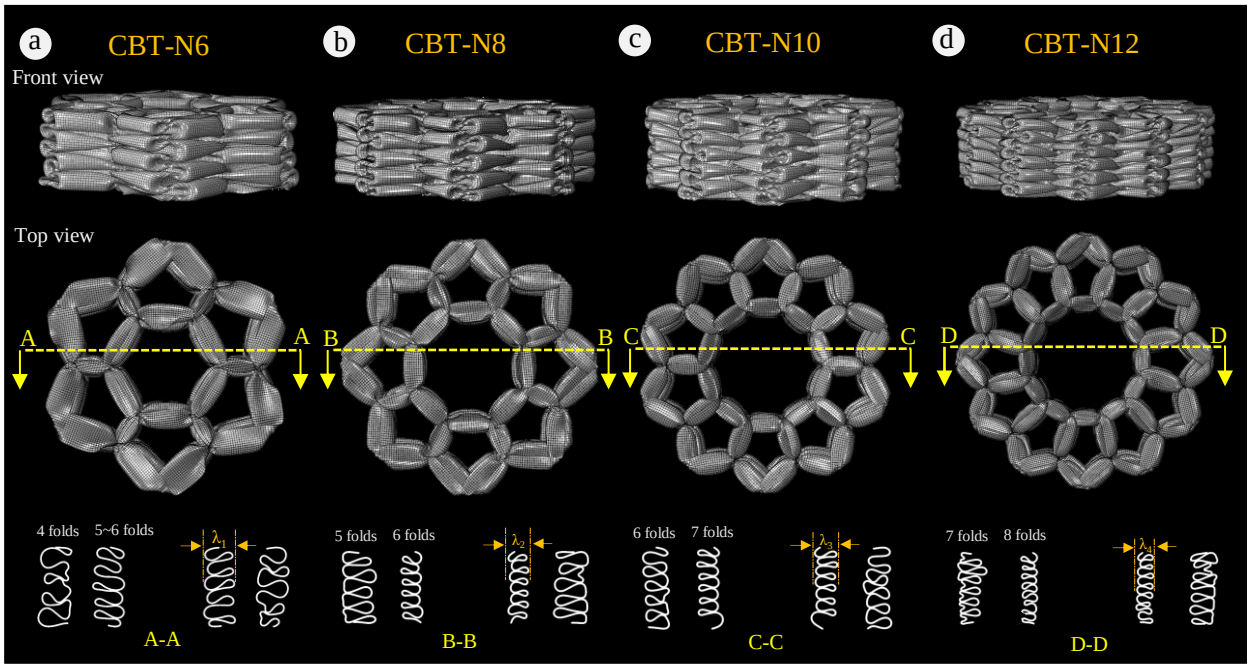

Fig.11. Deformation patterns and the profiles of CBTs with the same mass in Group A. (a)CBT-N6;(b) CBT-N8;(c) CBT-N10;(d) CBT-N12.

Fig.11 reveals that with an increase in *N*, the number of folded lobes also increases. Specifically, for *N* ranging from 6 to 12, the leftmost region of CBT produces 4, 5, 6, and 7 folds, respectively, while the number of folds in the leftmost and rightmost regions remains the same. In the middle region, the CBTs exhibit approximately 5.5, 6, 7, and 8 folds. Furthermore, the half wavelength of the folds decreases sequentially, i.e., $\lambda_4<\lambda_3<\lambda_2<\lambda_1$. Consequently, as *N* increases, more material within the CBTs undergoes plastic deformation, leading to an enhancement in the energy absorption efficiency of the structure.

The response curves of all groups exhibit similar trends, as shown in Fig.12. The force response curves of CBTs demonstrate three distinct stages: the initial crush stage, where the crushing force rapidly rises to the maximum peak force point, followed by a sharp decline into the crushing plateau stage characterized by stable energy absorption, and finally entering the densification stage. The fluctuation in the crush stage is relatively small, resulting in an overall stable energy absorption stage. From Fig.12, it is evident that the crushing force gradually increases with an increase in mass, as observed from Group A to Group D. Notably, the response curve levels for CBT-N8 and CBT-N10 are very similar in Groups A and B. Additionally, within the same group, the level of the response curves slightly increases as *N* increases, despite the wall thickness of the structure decreasing.

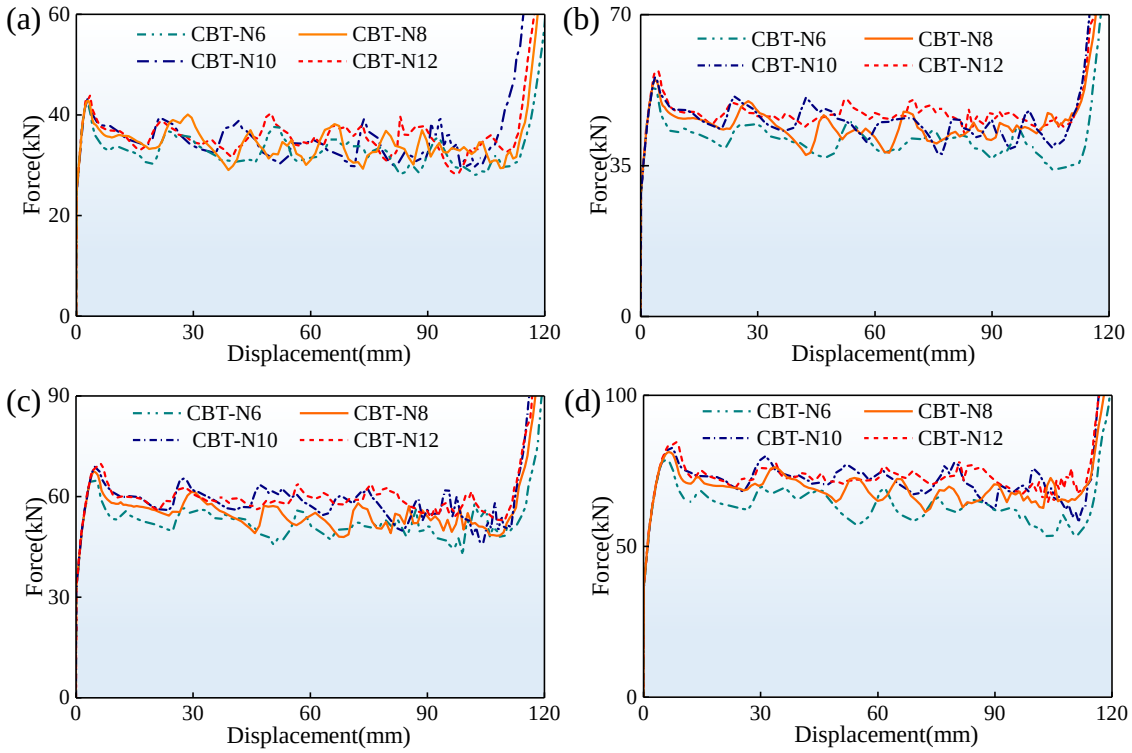

Fig.12. Force response curves of CBTs with the same mass. (a)Group A;(b) Group B;(c) Group C;(d) Group D.

Furthermore, the energy absorption performance of CBTs at a distance of d=110 mm is illustrated in Fig.13, while the corresponding data is provided in Table 3. In Fig.13a, the PCF exhibits a gradual increase from Group A to Group D. This can be attributed to the increase in tube wall thickness as the mass of the structure increases, resulting in a higher initial stiffness. However, within the same group, the PCF values remain relatively unchanged. This is due to the consistent cross-sectional area of the structure, which ensures that the initial stiffness remains essentially the same.

In Fig.13b, it is evident that the MCF slightly increases with N within each group. The MCF values of CBT-N6 and CBT-N8 are nearly equal in Groups A and B. However, in Groups C and D, the MCF of CBT-N12 is only marginally larger than that of CBT-N10. Specifically, the MCF values of CBT-N12 in Groups A to D are 35.01 kN, 46.8 kN, 59.45 kN, and 73.32 kN, respectively. Comparatively, the MCF of CBT-N12 is approximately 0.7%, 14.3%, 14.3%, and 14.5% higher than that of CBT-N6 from Groups A to D, respectively. Notably, CBT-N12 has a smaller wall thickness than CBT-N6 within the same group, and thus, CBT-N12 experiences a significant reduction in bending energy dissipated at the horizontal hinge line. However, due to the presence of more corners in CBT-N12, the energy dissipated by these corners outweighs the reduction in bending energy caused by the decrease in wall thickness. Consequently, CBT-N12 dissipates more energy

overall.

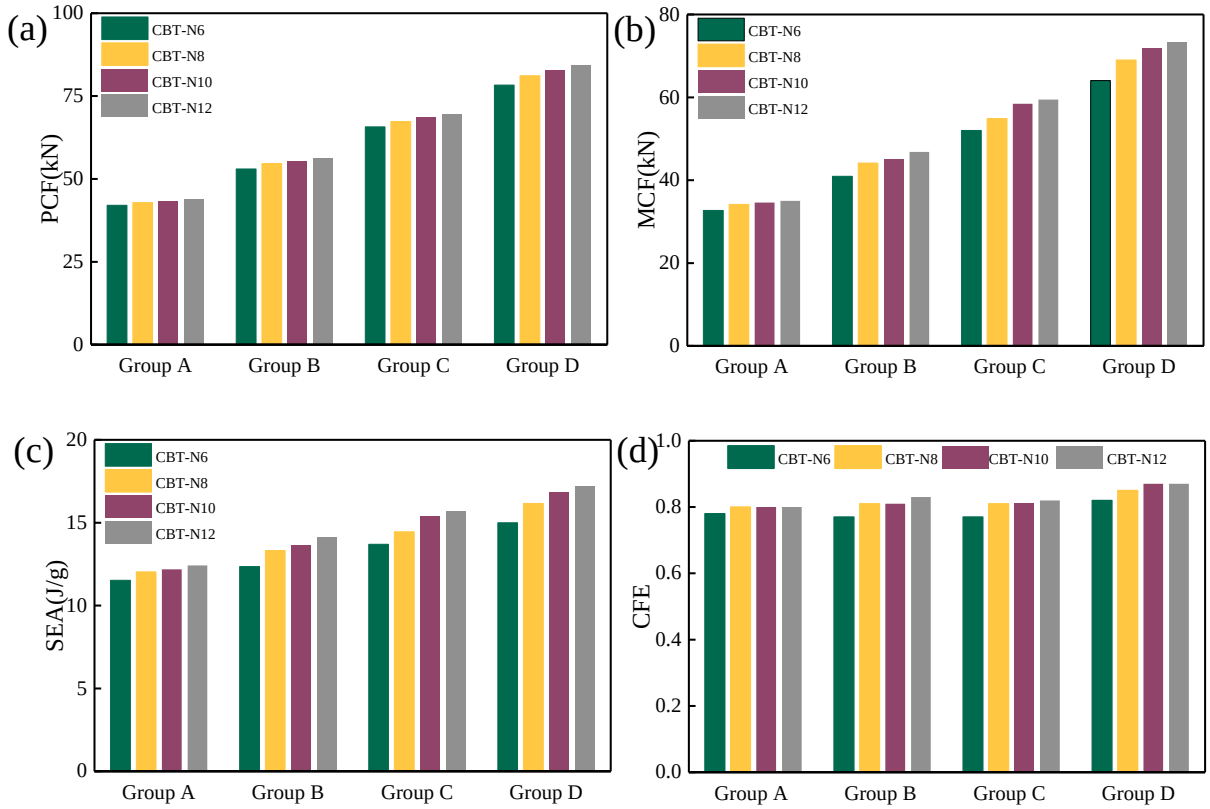

Fig.13. Energy absorption performance of CBTs with the same mass. (a)PCF;(b) MCF;(c) SEA;(d) CFE. overall.

Since the mass of the structures remains constant within the same group, the increasing trend and rate of MCF in each group are nearly identical to those of SEA, as illustrated in Fig.13c. The SEA of CBT-N12 in Groups A to D is 12.43 J/g, 14.12 J/g, 15.66 J/g, and 17.18 J/g, respectively, representing an approximate improvement of 7.9%, 14.3%, 14.3%, and 14.5% compared to the SEA of CBT-N6 in the corresponding groups. In Fig.13d, it can be observed that the CFE slightly increases with an increase in *N* within the same groups. Additionally, the CFE of CBT-N12 is approximately 1.02, 1.08, 1.06, and 1.06 times higher than that of CBT-N6 in the respective groups.

Within the same group, the energy absorption characteristics of CBTs display a notable similarity. As the parameter *N* increases, the energy absorption capacity of the structure shows only a slight improvement. Therefore, when considering structures with equal mass, it may be preferable to prioritize the use of CBT-N6 as an energy absorbing structure. This choice helps minimize the complexity and difficulty associated with structural manufacturing.

Table 3 The response performance of CBTs with the constant mass.

Group	Specimen	*t*(mm)	Mass(g)	PCF (kN)	MCF (kN)	SEA (kJ/kg)	EA (J)	CFE
Group A	CBT-N6	1.20	312.3	42.03	32.71	11.52	3598.38	0.78
	CBT-N8	1.07	312.3	42.85	34.17	12.03	3758.52	0.80
	CBT-N10	0.97	312.3	43.17	34.57	12.18	3802.74	0.80
	CBT-N12	0.90	312.3	43.86	35.01	12.43	3882.18	0.80
Group B	CBT-N6	1.40	364.5	53.03	40.94	12.35	4503.37	0.77
	CBT-N8	1.25	364.5	54.67	44.13	13.32	4854.3	0.81
	CBT-N10	1.13	364.5	55.40	45.10	13.61	4961.2	0.81
	CBT-N12	1.05	364.5	56.28	46.80	14.12	5148.45	0.83
Group C	CBT-N6	1.60	417.6	65.72	52.00	13.70	5720.91	0.77
	CBT-N8	1.43	417.6	67.33	54.87	14.45	6035.48	0.81
	CBT-N10	1.30	417.6	68.66	58.42	15.39	6426.46	0.81
	CBT-N12	1.20	417.6	69.42	59.45	15.66	6539.25	0.82
Group D	CBT-N6	1.80	469.53	78.31	64.06	15.00	7046.97	0.82
	CBT-N8	1.61	469.53	81.16	69.00	16.16	7589.95	0.85
	CBT-N10	1.46	469.53	82.85	71.73	16.80	7889.11	0.87
	CBT-N12	1.35	469.53	84.33	73.32	17.18	8064.74	0.87

4.2 Effect of structural wall thickness

In this section, we conducted an analysis of the crushing behavior of CBTs with a constant wall thickness. Our investigation focused on four groups, wherein each group consisted of structures with the same wall thickness. Consequently, the mass of each structure within the same group varied. The essential parameters for each group are summarized in Table 4.

Based on our numerical simulation analysis, we discovered that structures in all groups exhibit a desired progressive failure pattern. Since the deformation modes among different groups are generally similar, only Group D is presented as a representative in Fig.14. The deformed structures at the densification stage, showcasing the deformation shapes of CBTs with an inextensional pattern. As the value of *N* increases, there is a slight increase in the number of folded lobes. Specifically, in the case of CBT-N6 to CBT-N12, the leftmost flange produces 4, 4.5, 5, and 5 folds, respectively. Similarly, the middle region produces 5, 5.5, 6, and 6 folds, respectively. However, in the case of CBT-N10 and CBT-N12, despite having the same number of folds, there is an undeformed zone at the bottom of the middle section in CBT-N12, indicated by a green rectangular outline. Consequently, the relationship between half wavelength can be described as $\lambda_4<\lambda_3<\lambda_2<\lambda_1$.

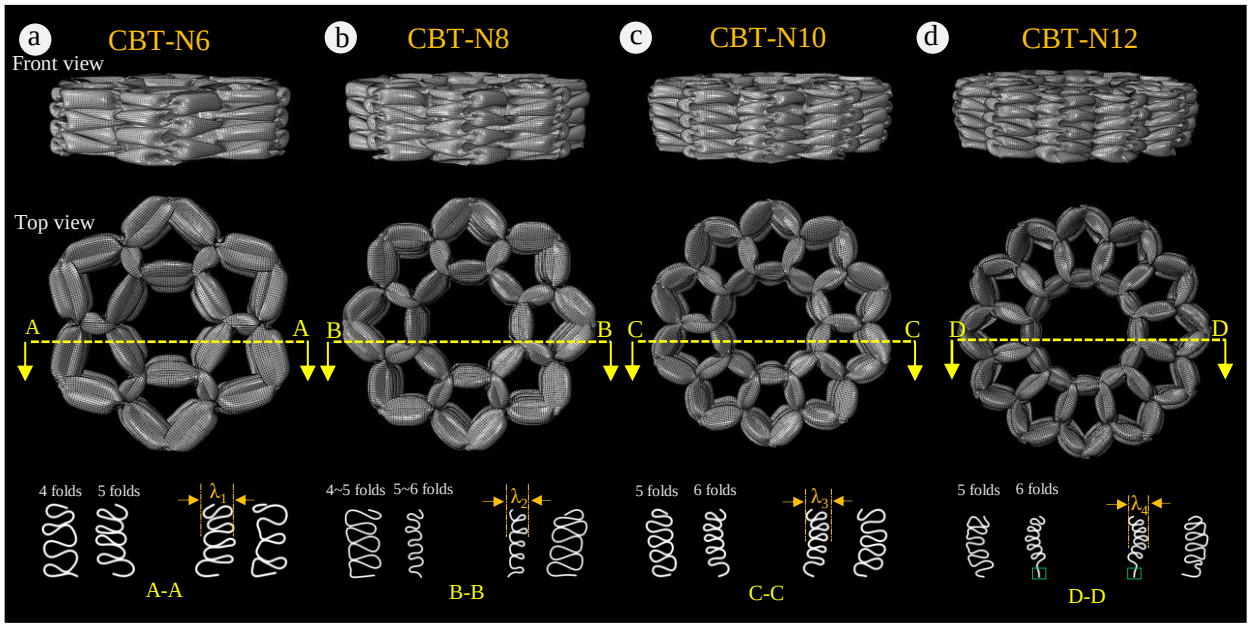

Fig.14. Deformation patterns and the profiles of CBTs with the same wall thickness in Group D. (a)CBT-N6;(b) CBT-N8;(c) CBT-N10;(d) CBT-N12.

Fig.15 illustrates the force response curves of CBTs, exhibiting distinct characteristics that can be categorized into three well-defined stages of crushing: the initial crush stage, the crushing plateau stage, and the densification stage, as elaborated in Section 3.2.1. When considering Group A to Group D, it becomes evident that the crushing force level of CBTs progressively increases with the growth in thickness, while maintaining a similar trend in the response curves. Among all the groups, CBT-N12 exhibits the highest level of crushing force and initial peak force, followed by CBT-N10, CBT-N8, and ultimately CBT-N6, which demonstrates the lowest force level.

Fig.16 depicts the energy absorption performance of the CBTs, specifically obtained at a distance of d=110 mm, with corresponding data provided in Table 4. Examining Fig.16a, it is evident that PCF exhibits a gradual increase with an increment in N. This can be attributed to the larger cross-sectional area of CBTs with higher N values, resulting in an increased initial stiffness of the structure. Consequently, a higher PCF is achieved.

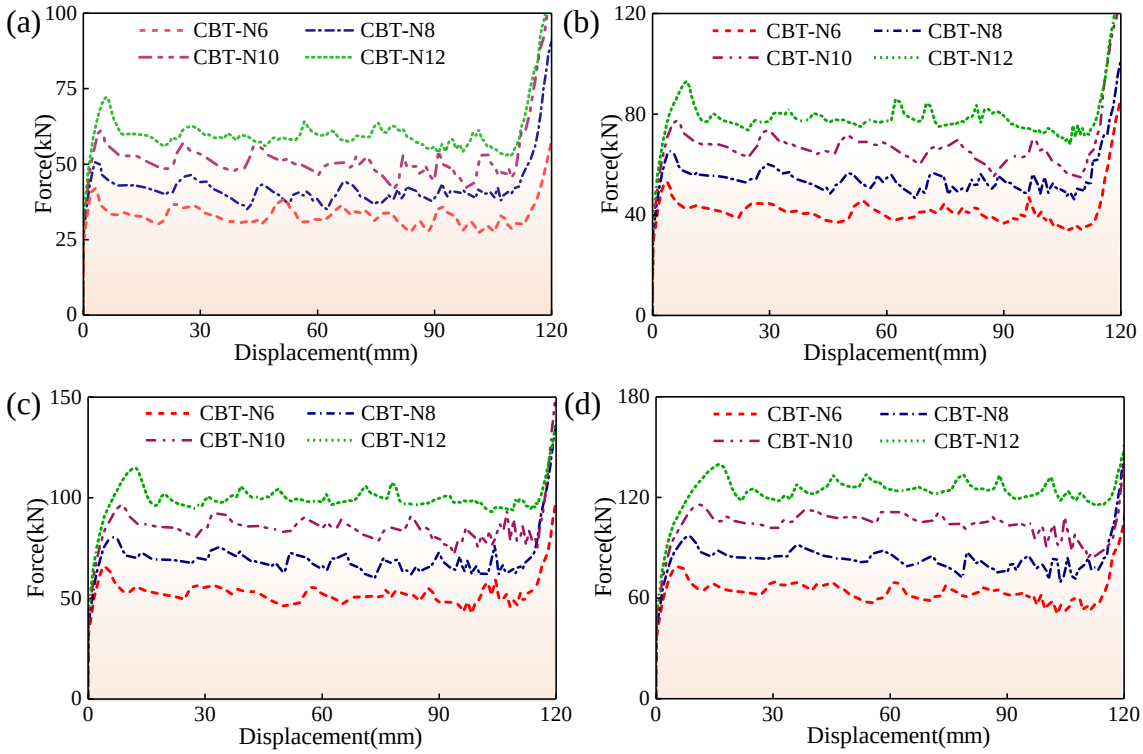

Fig.15. Force response curves of CBTs with the same wall thickness. (a)Group A;(b) Group B;(c) Group C;(d) Group D.

Furthermore, Fig.16b illustrates that the MCF in each group also shows a gradual increase as *N* increases. This behavior can be explained by the presence of additional corner elements in CBTs with larger *N* values. As a consequence, a larger crushing force is required to induce plastic deformation in these corner elements, consequently enhancing the overall crushing resistance of the structure.

Even though the mass of structures within the same group may vary, the specific energy absorption (SEA) serves as a crucial indicator for evaluating the energy absorption performance of the structure. Fig.16c demonstrates that CBT-N12 consistently achieves the highest SEA within each group, followed by CBT-N10, CBT-N8, and CBT-N6. Notably, CBT-N12 exhibits SEA values approximately 35.7%, 42.5%, 42.4%, and 45.6% higher than CBT-N6 in Groups A, B, C, and D, respectively. Moreover, it can be concluded that the SEA tends to gradually increase with an increase in thickness, progressing from Group A to Group D.

Across all groups, there is a slight increase in CFE as *N* increases from 6 to 10. However, when *N* reaches 12, the CFE starts to decrease, as illustrated in Fig.16d. Consequently, the CFE of CBT-N10 attains the highest value, approximately 5.1%, 7.7%, 7.5%, and 9.9% higher than CBT-N6 in Groups A, B, C, and D, respectively.

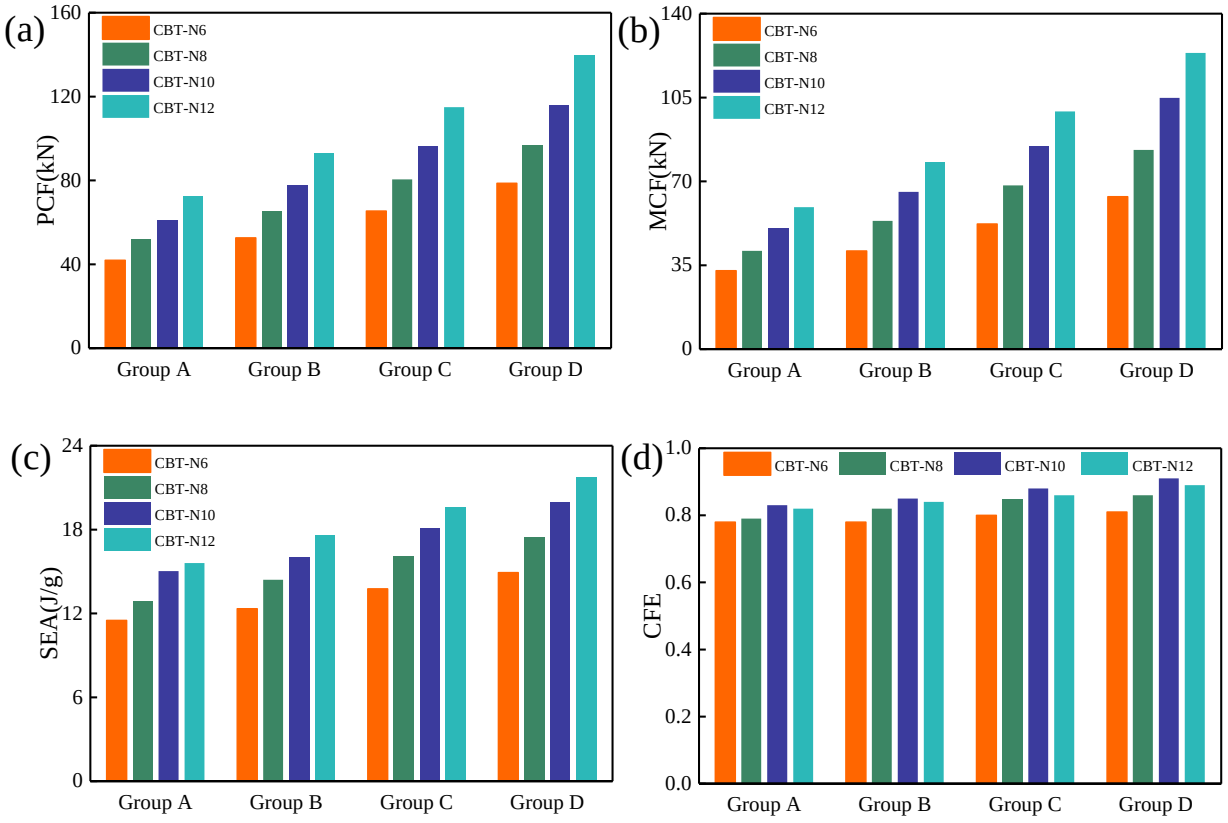

Fig. 16. Energy absorption performance for CBTs with constant wall thickness. (a)PCF;(b) MCF;(c) SEA; (d) CFE.

Table 4 The response performance of CBTs with the constant thickness.

Group	Specimen	*t*(mm)	Mass(g)	PCF (kN)	MCF (kN)	SEA (kJ/kg)	EA (J)	CFE
Group A	CBT-N6	1.2	282	41.90	32.71	11.50	3598.38	0.78
	CBT-N8	1.2	315	51.53	40.96	12.88	4505.24	0.79
	CBT-N10	1.2	347	60.85	50.28	15.03	5531.08	0.83
	CBT-N12	1.2	376	72.17	59.17	15.60	6508.88	0.82
Group B	CBT-N6	1.4	365	52.57	40.94	12.34	4503.37	0.78
	CBT-N8	1.4	408.2	65.27	53.44	14.40	5878.65	0.82
	CBT-N10	1.4	450.5	77.46	65.58	16.01	7214.23	0.85
	CBT-N12	1.4	487	92.83	77.82	17.58	8560.38	0.84
Group C	CBT-N6	1.6	417.2	65.40	52.19	13.76	5741.14	0.80
	CBT-N8	1.6	466.7	80.48	68.29	16.10	7511.63	0.85
	CBT-N10	1.6	514.8	96.19	84.70	18.10	9317.13	0.88
	CBT-N12	1.6	556.6	114.92	99.19	19.60	10910.50	0.86
Group D	CBT-N6	1.8	469.3	78.67	63.63	14.92	6999.73	0.81
	CBT-N8	1.8	524.8	96.57	83.08	17.41	9138.48	0.86
	CBT-N10	1.8	579.2	115.62	104.83	19.91	11531.80	0.91
	CBT-N12	1.8	626.1	139.62	123.63	21.72	13599.20	0.89

4.3 Effect of loading velocity

In practical crash scenarios, energy-absorbing structures invariably encounter dynamic loads. In this section, we delve into the dynamic response of the CBTs. The geometric parameters of the tubes remain consistent with the cases outlined in Section 3.1. A constant velocity is applied to the upper platen which compress the CBTs in the numerical simulation. To investigate the dynamic response, we utilize three distinct velocities: low velocity (V=20 m/s), medium velocity (V=50 m/s), and high velocity (V=80 m/s). These velocities provide insights into the structure's behavior across varying dynamic load conditions. Considering that energy-absorbing structures are typically affixed to components during service, a fixed boundary condition is implemented at the bottom of the structure for the dynamic loading scenarios.

The force response curves are depicted in Fig.17, with a comparison to the quasi-static cases selected from Section 3.1. Further details on energy absorption parameters are presented in Table 5, with these parameters being determined at a distance of d = 110 mm. Fig.17 visually highlights a substantial increase in both the PCF and the plateau crushing force as the crush speed escalates. This observation underscores the sensitivity of the force response curve to the rate of loading. Notably, the curves exhibit more pronounced fluctuation amplitudes at medium to high loading rates.

From the observations in Fig. 17, it is evident that the load curves exhibit more pronounced fluctuations after the initial peak force. To illustrate this phenomenon, we have selected CBT-N6 and CBT-N12 as representatives. Their response curves and corresponding deformation histories under impact loading at 80 m/s are detailed in Fig. S1 of the Supplementary Materials. Specifically, the buckling folds in both CBT-N6 and CBT-N12 initially appear at the impact end, primarily induced by the introduced indentation trigger. Subsequently, extensional folds gradually emerge at their distal ends, with the bulging folds intensifying as the loading persists.

In the case of CBT-N12, as the first extensional fold at the distal end approaches completion, localized buckling manifested at the impacted end. This occurrence coincides with a notable reduction in the load value, marked as point B1 on the response curve. Subsequently, the impacted end continues its movement towards the distal end, exhibiting progressive deformation. Simultaneously, the load curve displays near-periodic fluctuations. As the second extensional fold reaches completion at the distal end, an inward local buckling fold deformation occurs, leading to a significant drop in the load, reaching its nadir at point D.

For CBT-N6, as the extensional fold at the distal end nears completion, the load value on the response curve experiences a notable decrease, reaching point A. Subsequently, the impact end initiates the generation of a non-extensional fold, succeeded by the formation of a larger fold. This sequence leads to a relatively prolonged and smoothly loaded phase, spanning from point D to point B. Following this, localized buckling ensues, resulting in a continuous decline in the loads. It is evident that the significant perturbation of the load response curve is attributed to the switching and formation of various deformation modes.

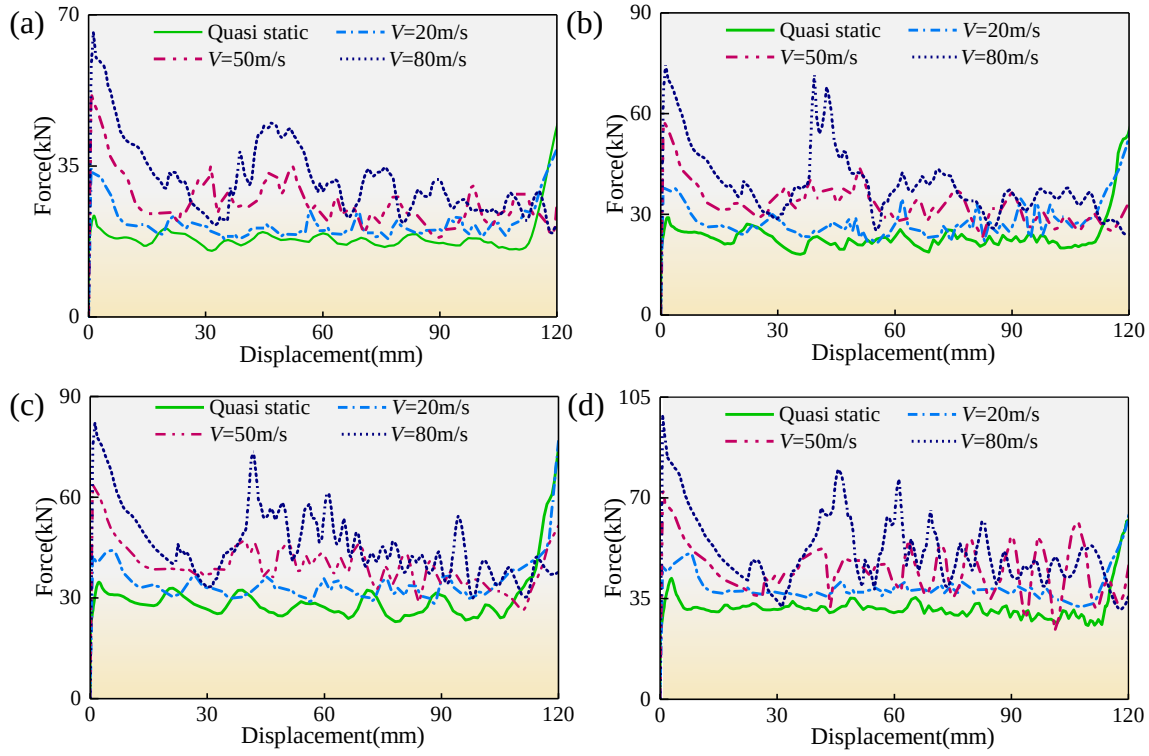

Fig.17. Force response curves of CBTs under different crushing velocities. (a)CBT-N6;(b) CBT-N8;(c) CBT-N10;(d) CBT-N12.

Analyzing Table 5, it becomes evident that the PCF values for CBT-N12, CBT-N10, CBT-N8, and

CBT-N6 experience marked increments of nearly 134.6%, 137.5%, 157.1%, and 181.1% respectively, when transitioning from quasi-static conditions to a loading speed of 80 m/s. Since aluminum alloy material isn't prone to strain rate sensitivity, the material's strain effect isn't considered within the numerical model. Consequently, the observed upsurge in PCF and crushing resistance force with increasing loading speed primarily attributes to the inertia effect exhibited by the structure.

Table 5 Energy absorption parameters of CBTs under different crushing speeds.

Specimen	Velocity (m/s)	PCF (kN)	MCF (kN)	SEA (kJ/kg)	EA (J)	CFE	Deformation mode
CBT-N6	Quasi static	23.40	17.85	9.84	1962.77	0.76	IBP
	20	34.67	21.00	11.58	2310.14	0.61	IBP
	50	51.70	26.94	14.86	2963.70	0.52	MDP
	80	65.78	32.63	17.99	3588.83	0.50	MDP
CBT-N8	Quasi static	29.00	22.52	11.10	2476.61	0.78	IBP
	20	38.47	27.05	13.34	2975.94	0.71	IBP
	50	57.14	33.28	16.41	3661.31	0.58	MDP
	80	74.57	39.91	19.68	4390.20	0.54	MDP
CBT-N10	Quasi static	34.60	27.84	12.44	3062.44	0.81	IBP
	20	42.67	33.57	15.00	3692.23	0.79	IBP
	50	63.43	39.63	17.71	4358.8	0.62	MDP
	80	82.19	46.88	20.95	5156.84	0.57	MDP
CBT-N12	Quasi static	42.00	31.40	12.96	3453.98	0.75	IBP
	20	46.78	38.27	15.79	4209.96	0.82	IBP
	50	73.22	45.78	18.89	5035.40	0.63	IBP
	80	98.55	52.50	21.66	5774.80	0.53	MDP

The dynamic deformation pattern is visually presented in Fig.18. In order to accentuate the characteristic deformation modes, select modes at different crush strains are chosen as representative illustrations. For V = 20 m/s, the structure consistently manifests an inextensional buckling pattern (IBP), akin to the behavior observed under quasi-static loading conditions. However, when the velocity exceeds or equals 50 m/s, a distinctive alteration is observed in the CBTs. Notably, multiple extensional fold lobes emerge, as indicated by the yellow dashed ellipses. This transformation leads the entire structure towards a mixed deformation pattern (MDP), characterized by the coexistence of inextensional and extensional folds. Particularly at higher loading velocities, CBTs exhibit a greater prevalence of extensional folded lobes, signifying an intensified manifestation of these deformation features.

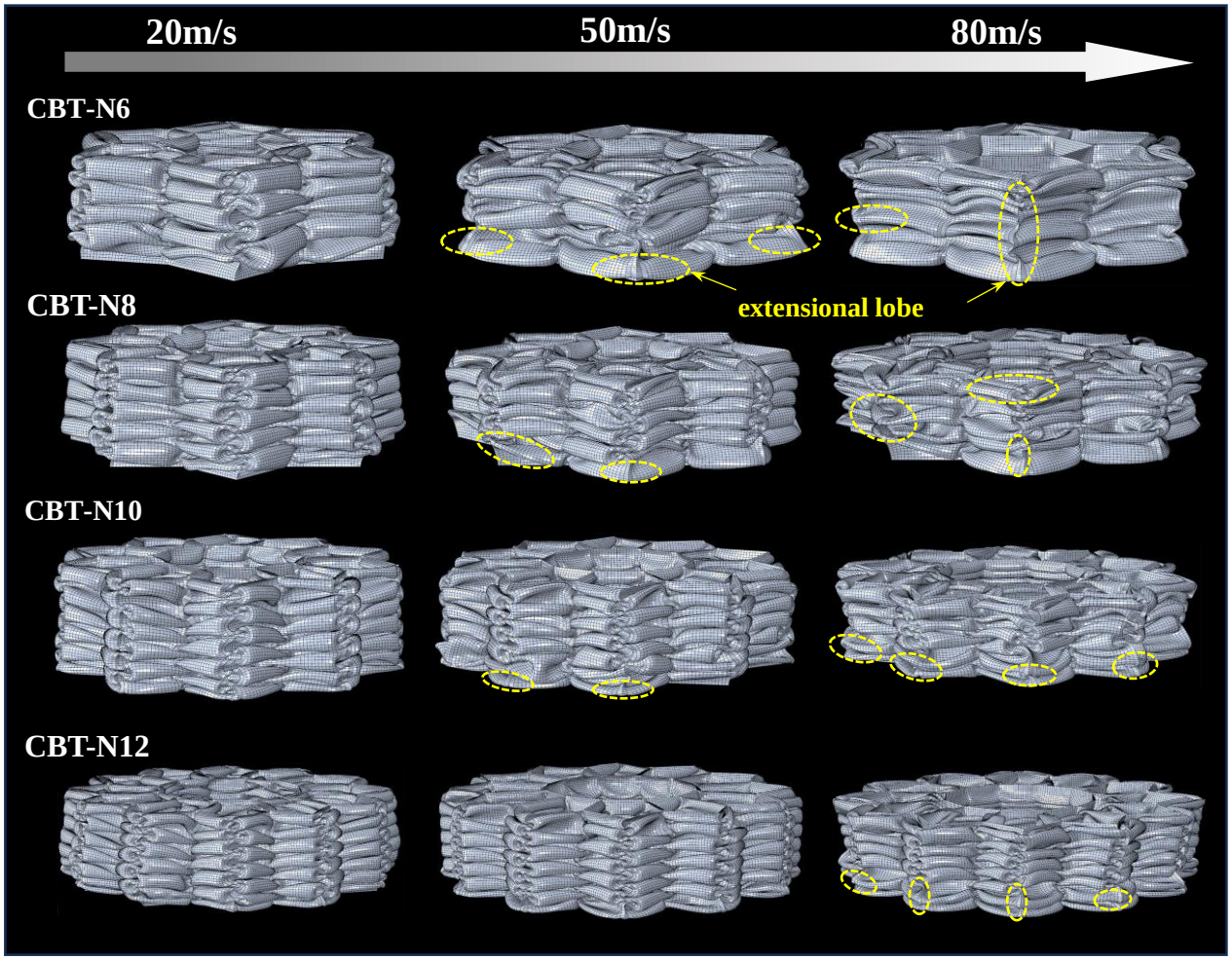

Fig.18. The deformation patterns of CBTs under different impact speeds.

Fig.19 illustrates that dynamic loading has a notable positive impact on both MCF and SEA, with a linear increase corresponding to loading speed. Particularly, the MCF of CBT-N12, CBT-N10, CBT-N8, and CBT-N6 experiences respective increments of 67.2%, 68.4%, 77.2%, and 82.8% as the crushing speed escalates

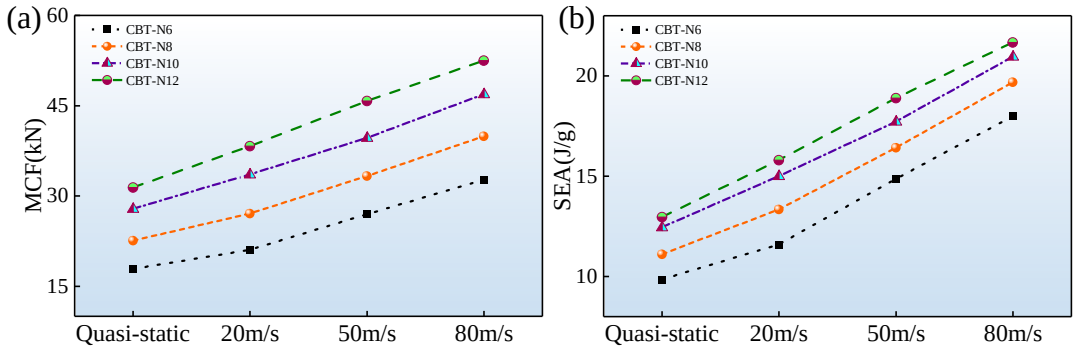

Fig.19. (a)MCF and (b) SEA of CBTs under diffferent crushing speeds.

from quasi-static to 80 m/s. This identical rate of increase is also mirrored in SEA. This observation underscores the sensitivity of CBTs' energy absorption performance to changes in crushing speed, indicating their heightened potential to effectively harness energy absorption capabilities under high-speed dynamic loading conditions.

4.4 Different cross-section configurations

This section further delves into the energy-absorbing traits of CBTs by introducing new structures characterized by distinct topological configurations labeled as Type A, B, and C. These configurations are devised based on the original CBTs' cross-sectional shapes (refer to Fig. 20). These newly introduced structures maintain identical outer and inner tube radii as the initially proposed CBTs, as elucidated in Section 2.1. The cross-sectional feature of the three newly derived structures is created by connecting the inner and outer tubes through ribs in distinct manners. Specifically, in Type A, the concave corner of the outer tube is connected to the midpoint of the inner tube wall via ribs. In Type B, the convex corner of the outer tube is linked to the midpoint of the inner tube wall through ribs. In Type C, the convex corner of the outer tube is connected to the corner of the inner tube via ribs. Additionally, they possess a uniform wall thickness of 0.85 mm and a height of 150 mm. The comprehensive geometric parameters of these new structures are meticulously detailed in Table 6. For the sake of simplicity in nomenclature, structures such as TA-CBT-N6 signify CBT-N6 within Type A, where "TA" abbreviates Type A. Correspondingly, "TB" and "TC" abbreviations denote Type B and Type C, respectively. As for the original CBTs presented in Section 2.1, they are designated as O-CBT-N6 within this section, wherein the letter "O" indicates "original."

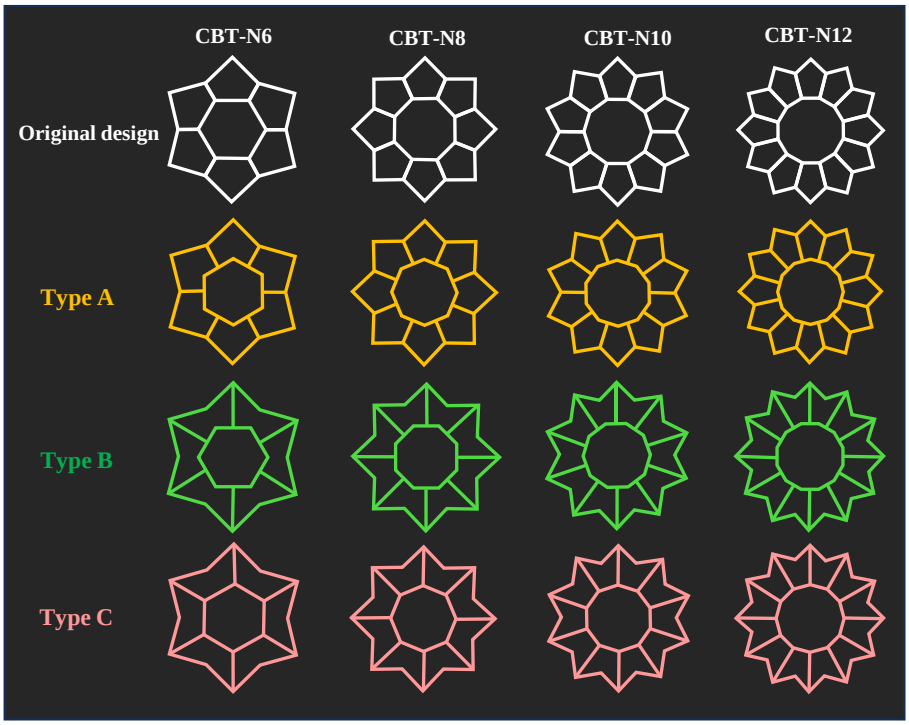

Fig.20. Illustration of the derived CBTs with three different cross-section configuration types.

Table 6 The parameters of side length for the new CBTs in the different types.

	Side length(mm)	CBT-N6	CBT-N8	CBT-N10	CBT-N12
Type A, B,C	L_i	25	19.13	15.45	12.68
	L_o	28.28	22.57	18.9	16.13
Type A	L_r	18.35	18.63	19.50	20.33
Type B	L_r	33	31.4	30.72	30.34
Type C	L_r	29.64	29.50	29.50	29.51

Upon examination, these newly introduced structures consistently display a progressive buckling mode, as evidenced in Fig.21. Specifically, the outer tube assumes a pattern of regular inextensional folds. These folded lobes undergo a modest augmentation as N increases. Notably, among all the new CBTs, TA-CBT-N12 boasts the highest count of seven folds, setting a record for the maximum number of lobes. Comparatively, the number of folds in CBTs of Types B and C remains largely similar. In the context of Type A and Type B structures, inner tubes from CBT-N8 to N12 demonstrate the emergence of irregular folds. These unique deformations are conspicuously highlighted within white-colored circles in Fig.21.

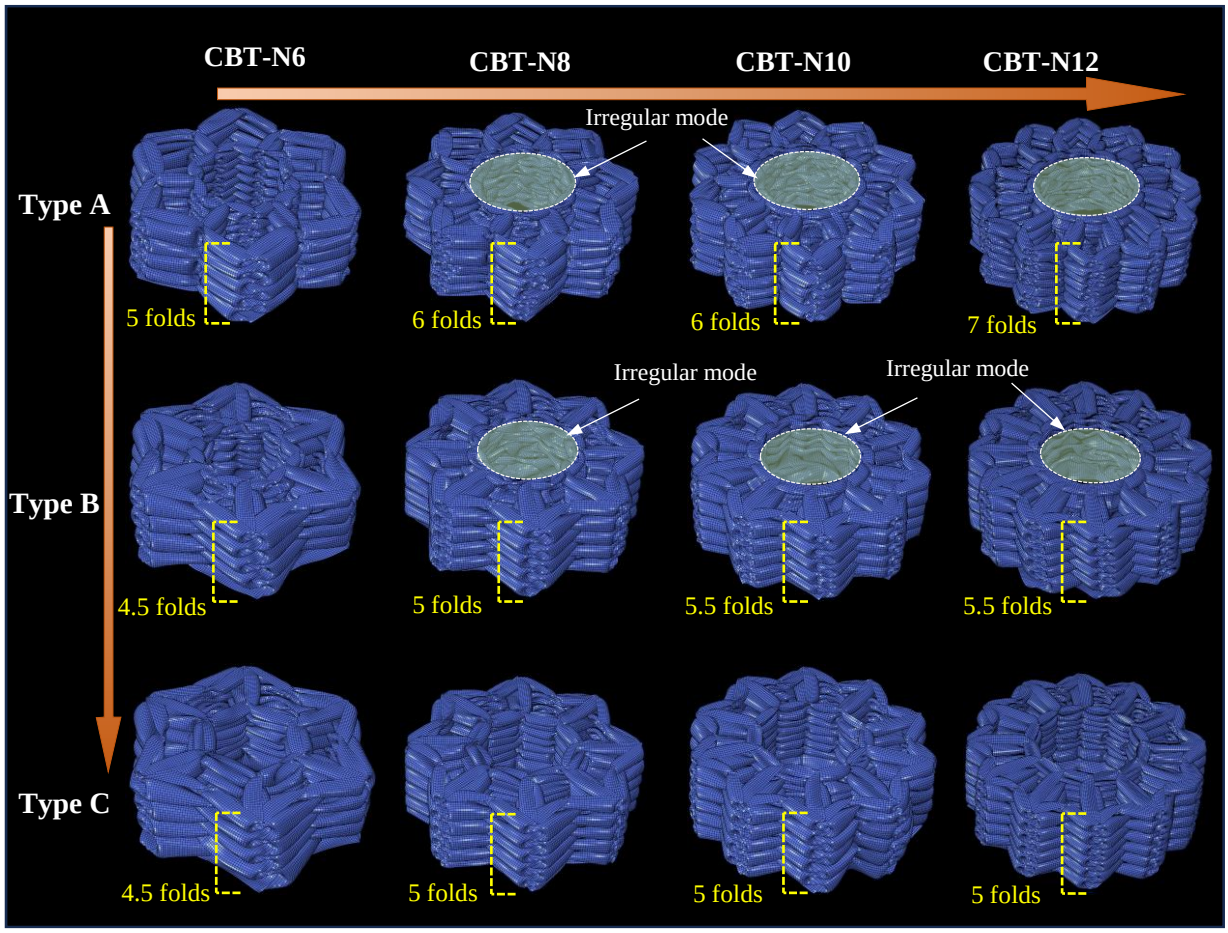

Fig.21. Deformation pattern of the derived CBTs in the three types under quasi static axial crushing.

This intriguing phenomenon primarily stems from the intricate deformation mechanisms unfolding at the intersection nodes between the rib plates and the inner tubes. In stark contrast, CBTs belonging to Type C consistently exhibit a uniform and regular deformation mode across all inner tubes.

The graphs illustrating the response curves can be found in Figs.22a to 22c. Similar trends are noticeable in these curves across various types. The response parameters, which were computed for a crushing displacement of 110 mm, are listed in Table 7 as well. Among each specific type, CBT-N12 shows the greatest initial peak force and crushing force. Fig.22d illustrates that the MCF of CBTs in Type A surpasses that of the other types. Furthermore, within each type, an increase in N leads to a corresponding increase in MCF.

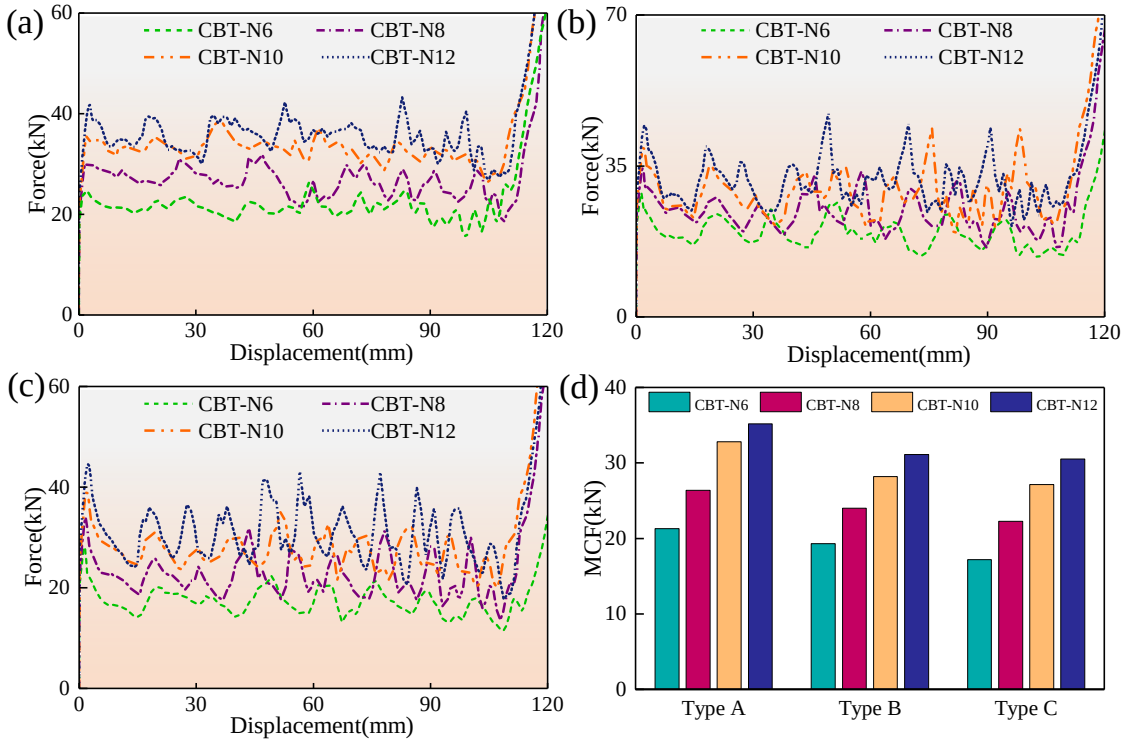

Fig.22. Force response curves for the derived CBTs in (a)Type A, (b)Type B and (c)Type C. (d)MCF for the derived CBTs.

The SEA data is displayed in Fig.23a. Among all the CBTs, TA-CBT-N12 and TA-CBT-N10 show higher SEA values. Additionally, the SEA of TA-CBT-N10 (14.41J/g) is slightly 1.5% greater than that of TA-CBT-N12(14.20J/g). Furthermore, when compared to the original CBTs, the SEA value of TA-CBT-10 surpasses O-CBT-N10(12.44J/g) by approximately 15.84%. This emphasizes the possibility of enhancing energy absorption efficiency through suitable adjustments in topological configuration of the bionic structure.

Among each type, CBT-N10 exhibits the highest CFE as depicted in Fig.23b. Furthermore, Type A maintains an advantage in CFE compared to the other types. To be specific, the CFE of TA-CBT-N10 surpasses that of TB-CBT-N10 by approximately 27.78% and exceeds TC-CBT-N10 by approximately 31.43%.

Type A structures, forming 5~7 folds compared to the 4.5～5 folds in other types (refer to Fig. 21), demonstrate heightened plastic deformation energy dissipation. Additionally, the interaction of ribs with the inner tube in Type A results in a more intricate and severe deformation, contributing to a notable increase in energy dissipation. The crush resistance of the three-plate element, formed by connecting ribs to the outer tube in Type A, surpasses

that of the corresponding elements in Types B and C. Furthermore, structures in Type A exhibit a smaller mass than their counterparts in the other types, as detailed in Table 7. The amalgamation of these factors establishes the superior energy-absorbing properties of Type A structures in comparison to other types.

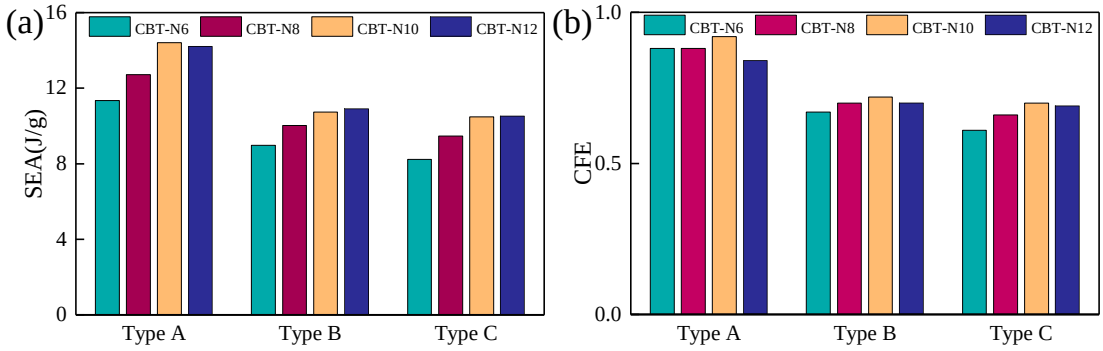

Fig.23. (a)SEA and (b) CFE for the derived CBTs.

Table 7 Response parameters of the derived CBTs.

	Specimen	*t*(mm)	PCF (kN)	MCF (kN)	SEA (kJ/kg)	EA (J)	CFE	Mass(g)
Type A	CBT-N6	0.85	24.31	21.28	11.34	2340.90	0.88	206.42
	CBT-N8	0.85	30.16	26.39	12.71	2902.86	0.88	228.39
	CBT-N10	0.85	35.56	32.80	14.41	3608.28	0.92	250.40
	CBT-N12	0.85	41.71	35.17	14.20	3869.16	0.84	272.48
Type B	CBT-N6	0.85	28.67	19.30	8.97	2122.57	0.67	236.63
	CBT-N8	0.85	34.30	24.00	10.02	2639.33	0.70	263.41
	CBT-N10	0.85	39.33	28.20	10.73	3102.43	0.72	289.14
	CBT-N12	0.85	44.29	31.10	10.90	3420.92	0.70	313.85
Type C	CBT-N6	0.85	28.06	17.18	8.23	1890.15	0.61	229.67
	CBT-N8	0.85	33.71	22.25	9.47	2447.34	0.66	258.43
	CBT-N10	0.85	38.67	27.13	10.48	2984.02	0.70	284.73
	CBT-N12	0.85	44.44	30.53	10.52	3359.04	0.69	319.30

5. Theoretical analysis

In this section, theoretical analysis is performed to predict the crushing response force of CBTs, which provides a deeper understanding of the energy-absorbing mechanism as well as a rapid assessment of the performance of the structures. It is assumed that the material exhibits perfect rigid-plastic behavior, and the work performed by the external force on the structure is entirely converted into energy dissipation through

the plastic deformation of the material. Thus, the equilibrium equation in generating a complete folding process can be expressed as follows,

$$2HP_m\kappa = W_{bending} + W_{membrane} \tag{5}$$

where P_m is the MCF, denotes the mean crush resistance force, and H represents the half-wavelength of a fold. κ is the crush displacement coefficient, which is set at 0.7 according to the experimental results. $W_{bending}$ and $W_{membrane}$ is bending and membrane deformation energy, respectively.

5.1 Bending energy

As Fig.24 [59] illustrates the bending deformation process of a flange plate, the dissipated bending energy of the plastic hinge line can be evaluated as,

$$W_{bending} = \sum_{i=1}^{3} \theta_i M l \tag{6}$$

where θ_i is the rotation angle of hinge lines, l is the length of the flange plate. M is the plastic bending moment, as follow:

$$M = \frac{\sigma_0 t^2}{4} \tag{7}$$

where σ_0 and t are the equivalent plastic flow stress of material and the thickness of the flange, respectively. To determine more realistic the plastic flow stress, the stress σ_0 is decided according to energy equivalence method as follow[60]:

$$\sigma_0 = \frac{\left(\int_0^{\varepsilon_0} \sigma \mathrm{d}\varepsilon\right)}{\varepsilon_0} \tag{8}$$

where σ_u refers to the ultimate tensile strength of the material. ε_0 denotes the strain corresponding to σ_u. By the experiment, $\varepsilon_0 = 0.23$, and thus $\sigma_0 = 77\text{MPa}$.

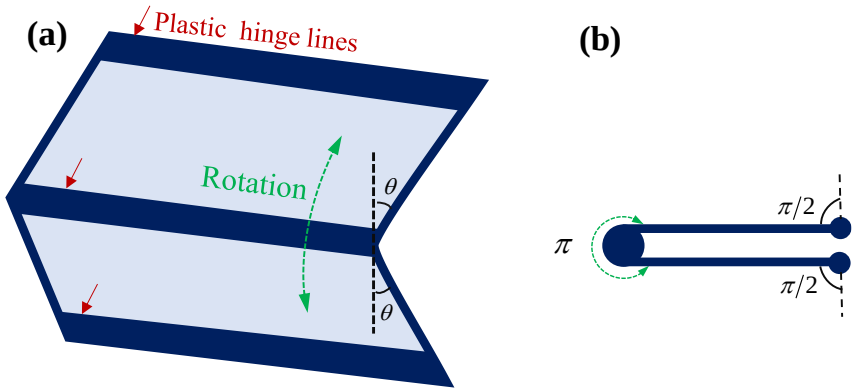

Fig.24. Illustration of flange bending energy dissipation. (a) Bending deformation (b) Side view after deformation.

5.2 Membrane energy

For a more comprehensive analysis of membrane deformation energy, the cross-section of CTBs is subdivided into constituent elements, as illustrated in Fig. 25a. There are three types of constitutive elements including corner element-shape element(I) and Y-shape element (II). As depicted in Fig.25a, each type comprises six elements in CBT-N6, eight elements in CBT-N8, ten elements in CBT-N10, and twelve elements in CBT-N12. The deformation patterns of these elements are ascertained based on both experimental and numerical outcomes outlined in Section 3.1, with a schematic representation provided in Fig.25b. The prototypical deformation mode for these elements is also depicted in Fig. 26

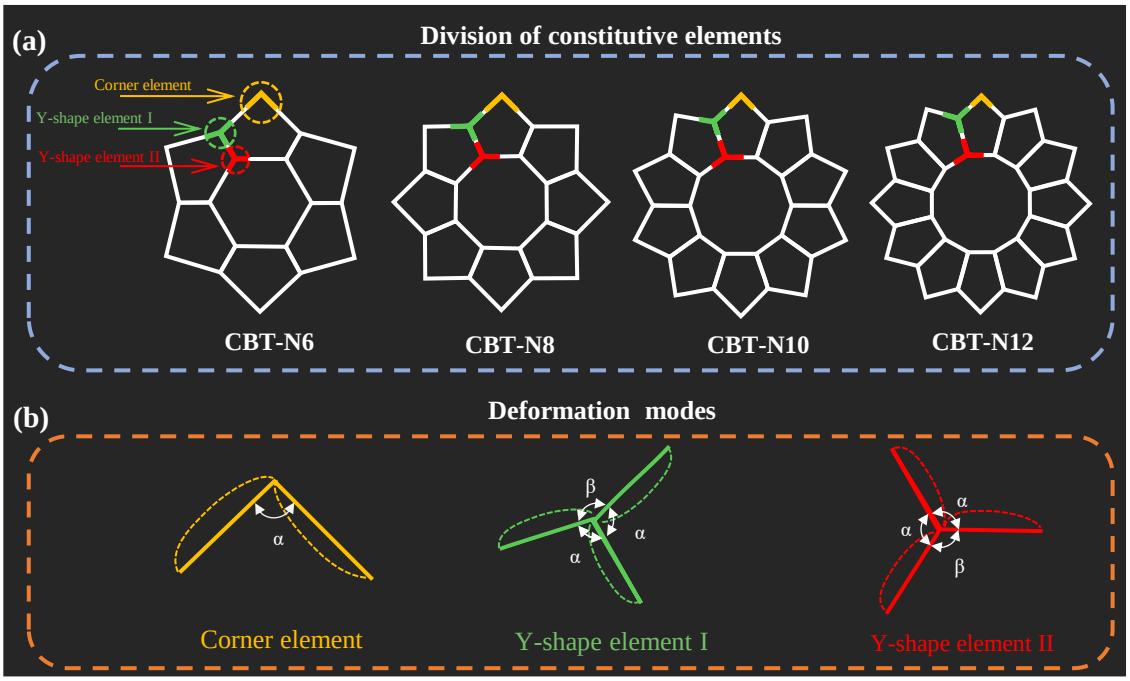

Fig.25. Diagram of constitutive elements of CBTs and deformation modes of the elements.

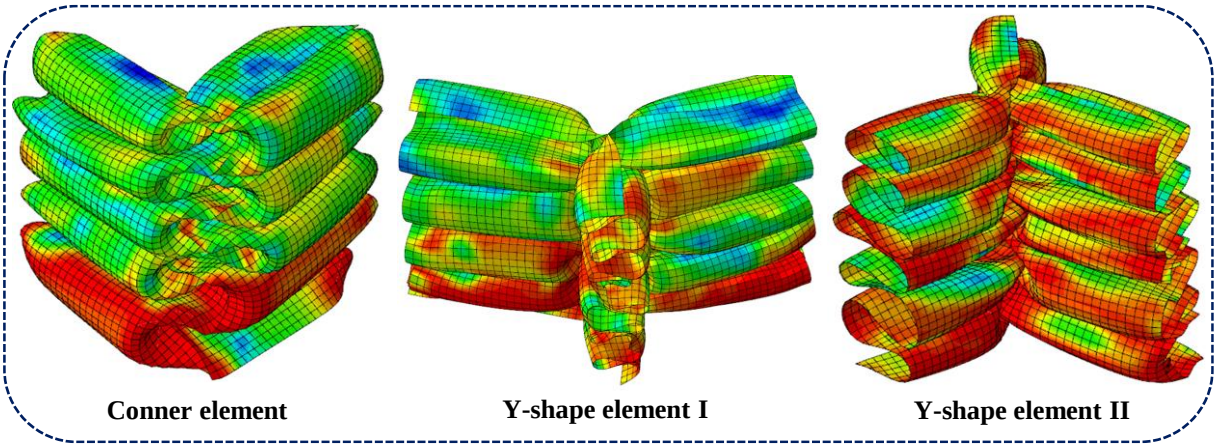

Fig.26. The representative deformation modes of the constitutive elements.

Furthermore, the membrane energy dissipation of the constitutive elements is analyzed here. For a corner element with an angle α_0, the membrane energy is [61] ,

$$W_{membrane}^{conner} = \frac{4MH^2}{t} \frac{tan(\alpha_0/2)}{0.164(B/t)^{0.6}\left(tan(\alpha_0/2)+0.06/tan(\alpha_0/2)\right)} \tag{9}$$

where B denotes the width of flange.

For a Y-shape element (I), as depicted in Figs.25b and 26, each of flanges in the Y-shape element I is collapsed in the same direction, the energy dissipated by this element can be expressed as follow [62],

$$W_{membrane}^{Y-I} = \frac{4MH^2}{t}\left(\frac{tan(\alpha_1/2)}{0.164(B/t)^{0.6}\left(tan(\alpha_1/2)+0.06/tan(\alpha_1/2)\right)}+2tan\left(\alpha_1/2\right)\right) \tag{10}$$

where α_1 denotes center angles of the element.

In the case of a Y-shape element (II), one of the flanges collapses in a direction opposite to the other two flanges, as illustrated in Figs.25b and 26. As a result, the energy dissipation of this element can be calculated as per the formula derived in reference [62],which is given by

$$W_{membrane}^{Y-II} = \frac{2MH^2}{t}\left(4tan\left(\beta/4\right)+2sin\left(\beta/2\right)+3sin\beta\right) \tag{11}$$

where β represents the angle of flanges, as depicted in Fig.25b.

5.3 Mean crushing force

According to Fig.25a, the CBT-N6 is composed of six elements each of type conner element, Y-shape element (I) and Y-shape element (II). Thus, the the mean crushing force (MCF) of the CBT-N6 can be written according to Eq. (5), as follow:

$$2HP_m\kappa = 2\pi Ml + 6W_{membrane}^{conner} + 6W_{membrane}^{Y-I} + 6W_{membrane}^{Y-II} \tag{12}$$

In addition, the following results can further be derived,

$$\frac{P_m}{M} = \frac{1}{\kappa}\left[\frac{\pi l}{H} + \frac{6H}{t}\left(\begin{array}{l} \dfrac{2\tan(\alpha_0/2)}{0.164(B_0/t)^{0.6}\left(\tan(\alpha_0/2)+0.06/\tan(\alpha_0/2)\right)} + \\ \dfrac{\tan(\alpha_1/2)}{0.164(B_1/t)^{0.6}\left(\tan(\alpha_1/2)+0.06/\tan(\alpha_1/2)\right)} \\ +4\tan(\alpha_1/2)+4\tan(\beta/4)+2\sin(\beta/2)+3\sin\beta \end{array}\right)\right. \tag{13}$$

The value of α_0 and α_1 is $\pi/2$, $7\pi/12$ in the conner element and Y-shape element (I), respectively. β is $\pi/3$ in Y-shape element (II). l represents the overall length of the flanges and is 579.36 mm for the CBT-N6. B_0 is 14.14mm and the average B_1 is 11.93mm. According to the principle of minimum energy, the half-wavelength H can be determined by $\delta P_m/\delta H = 0$, then

$$H = \sqrt{\frac{\pi tl}{95.48}} \tag{14}$$

Furthermore, MCF of CBT-N6 can be expressed as follow:

$$P_m = \frac{\pi l\sigma_0}{2H\kappa}t^2 \tag{15}$$

Similarly, theoretical models of MCF can be established for CBT-N8, CBT-N10 and CBT-N12, respectively. As follows,

CBT-N8:

$$P_m = \frac{324.04\pi\sigma_0}{H\kappa}t^2 \tag{16}$$

where the half wavelength $H = \sqrt{\pi tl/141.24}$, l is 648.08mm for CBT-N8.

CBT-N10:

$$P_m = \frac{357.5\pi\sigma_0}{H\kappa}t^2 \tag{17}$$

where the half wavelength $H = \sqrt{\pi tl/215.9}$,l is 715 mm for CBT-N10.

CBT-N12:

$$P_m = \frac{389.52\pi\sigma_0}{H\kappa}t^2 \tag{18}$$

where the half wavelength $H = \sqrt{\pi tl/260.2}$,l is 779.04 mm for CBT-N12.

Table 8 The theoretical and numerical MCF values of CBTs.

Specimen	Theoretical results(kN)	Numerical results(kN)	Difference (%)
CBT-N6	17.98	17.85	+0.7
CBT-N8	23.10	22.52	+2.6
CBT-N10	30.04	27.84	+7.9
CBT-N12	34.35	31.40	+9.4

Table 8 indicates that the disparities between theoretical and numerical results are 0.7%,2.6%, 7.9% and 9.4%, respectively. Consequently, the theoretical and numerical MCF values exhibit a notable concurrence, underscoring the accuracy of the theoretical model in predicting MCF.

Furthermore, the results of theoretical and numerical MCFs for CBTs with different thicknesses are displayed in Fig.27.It can be seen that when the thickness is less than or equal to 1.6mm, the theoretical and numerical results match more closely, and when the thickness is 1.8mm, some slight deviation occurs. Overall, the theoretical and numerical results have a good match. Note that due to the fact that the effective distance coefficient K decreases as the thickness of the structure and the number of folds increase. Thus, for the theoretical analysis, K in CBT-N6 was determined to be 0.67 and set to 0.66 in CBT-N8, CBT-N10, and CBT-N12 to provide a more reasonable assessment of the mean crushing force.

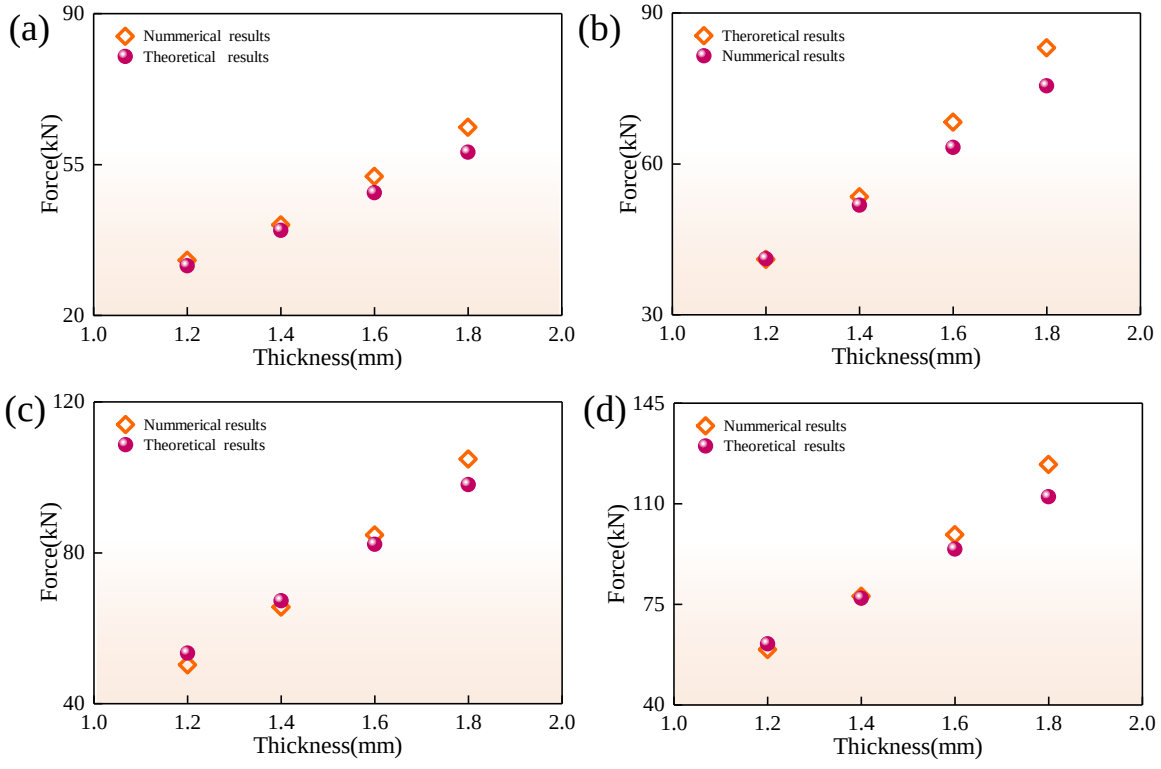

Fig.27. Theoretical and numerical MCFs for (a)CBT-N6, (B)CBT-N8, (C)CBT-N10, and (D)CBT-N12 with various thickness.

6. Comparison of performance with classic energy absorbing structures

To further underscore the superior energy-absorbing properties of CBTs, a comprehensive performance assessment was conducted by comparing them with other competitive multi-cell tubes and recently introduced bioinspired thin-walled structures. These structures include the triple-cell square tube(TST)[59], quadruple-cell square tube I(QST-I)[63], quadruple-cell square tube II(QST-II) [63], five-cell square tube(FST)[64], bio-inspired hierarchical square tube (BHST)[48], multi-cell double square tube (MDST)[65],anti-tetrachiral square tube(ATST)[66],triple-cell circular tube(TCT)[67],quadruple-cell circular tube(QCT)[67], multi-cell bicircular tube(MBT)[68], horsetail bionic structure(HBS)[44], bio-inspired fractal multi-cell circular tube(BFMCT)[69], bio-inspired hierarchical multi-cell bi-tubular tube(BHMBT)[70],bio-inspired pentagonal structure(BPS)[71], multi-cell hexagonal tube (MHT)[72], six-cell hexagonal tube(SHT)[73], bio-inspired hexagonal structure(BHS)[71], bio-inspired hierarchical multi-cell hexagonal tube(BHMHT)[47], hierarchical multi-cell hexagonal tube(HMHT)[74], self-similar inspired multi-cell tube(SIMT)[75].Importantly, these structures share the identical external circular diameter(109mm), height(150mm), and mass (199.44g) with CBTs. Thus, the wall thickness t for these structures is variant. The essential geometric parameters of these structures are shown in Fig.28. To ensure a fair comparison, these structures employ the same material parameters as those of the CBTs (as shown in Fig.3a).

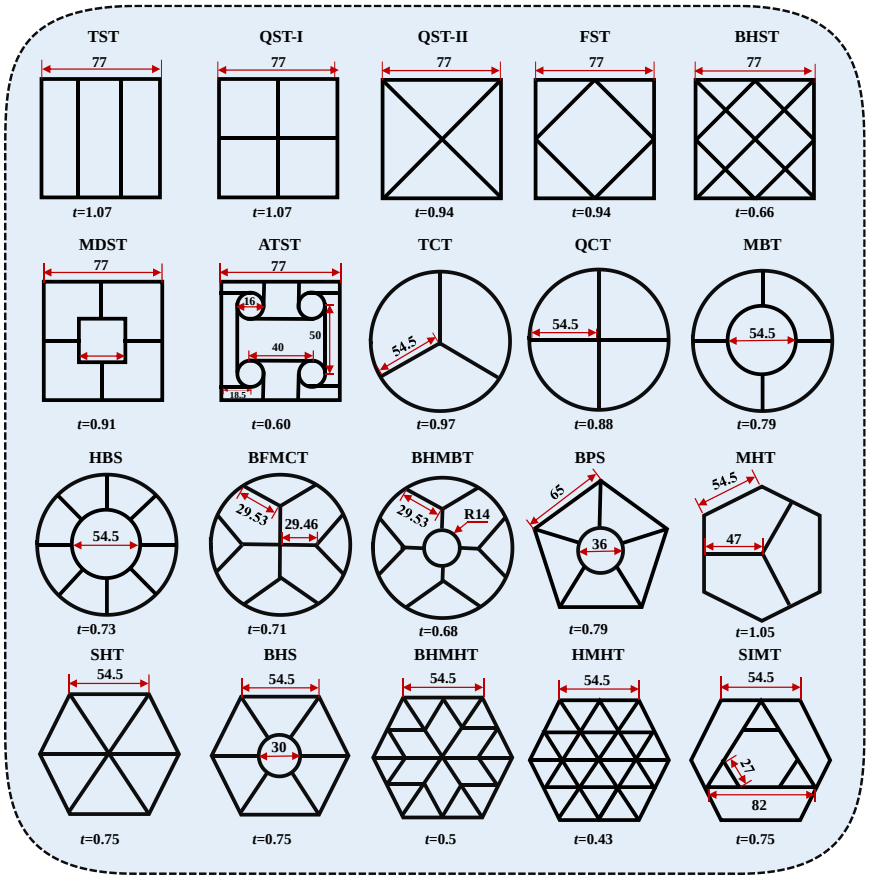

Fig.28. Geometrical specifications of various newly bionic and typical multi-cell structures.

Extensive numerical simulations were performed to evaluate the energy absorption parameters at a compression displacement of d=110 mm. Then failure modes and energy absorption performances of the structures are summarized in Table 9, indicating that the structures exhibit a progressive buckling mode. The SEA values for CBT-N6 to N12 are recorded as 9.84J/g,10.5J/g,11.44J/g, and 11.36J/g, respectively. Correspondingly, the CFE for CBT-N6 to CBT-N12 is calculated as 0.76,0.78,0.85, and 0.82, respectively. The comparative outcomes between CBTs and well-known energy-absorbing structures in terms of SEA and CFE are presented in Fig.29. The deformation patterns and energy absorption properties of the typical structures are presented in Appendix Table A1.

The CBTs demonstrate notably elevated SEA values, with CBT-N10 showcasing a remarkable 11.44 J/g, which surpasses the highest (8.92 J/g) and lowest (5.02 J/g) SEA values of the compared structures by approximately 28.3% and 127.9%, respectively. As such, the CBTs stand out as lightweight energy-absorbing structures possessing exceptional energy-absorbing attributes, can maximize the energy-absorbing performance of the materials. Consequently, these structures hold the potential to supplant traditional counterparts across diverse engineering applications.

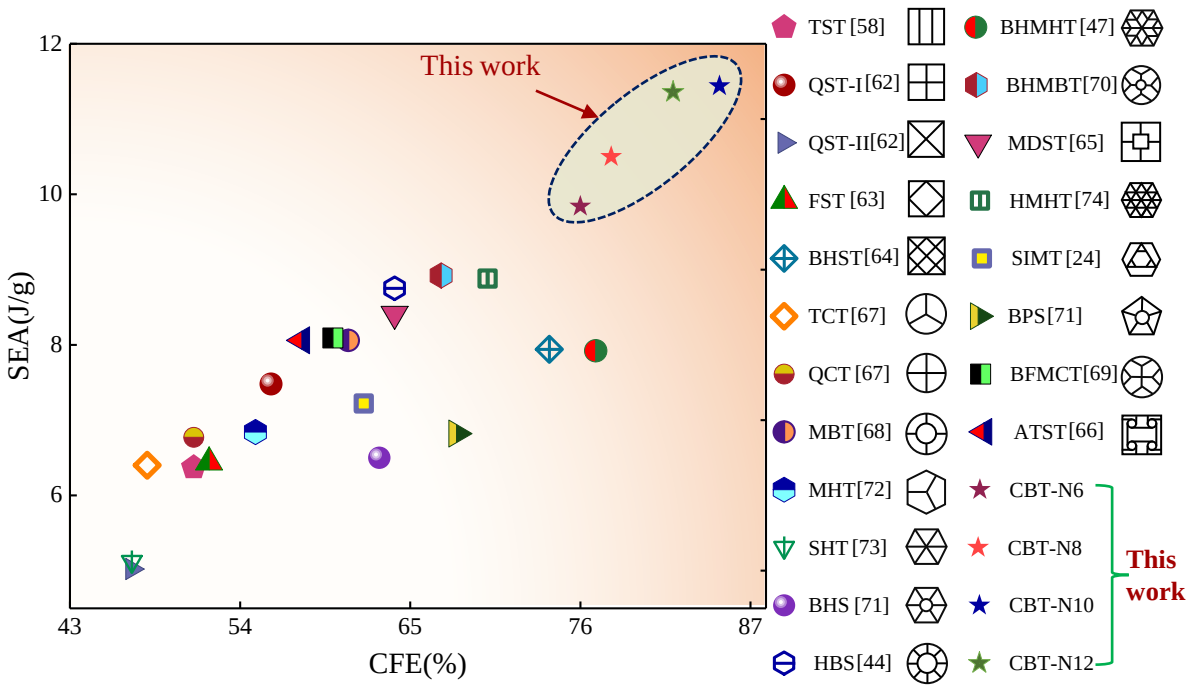

Fig.29. Comparing the SEA and CFE for CBTs and typical energy absorbing multi-cell structures under the same mass.

7. Conclusions

This study introduces innovative cactus-inspired bionic tubes (CBTs) with exceptional energy-absorbing capabilities. A high-fidelity numerical model, rigorously validated using experimental data, is employed to analyze the energy-absorbing characteristics of CBTs. SEA demonstrates heightened sensitivity to changes in the number of corners (N) under uniform structural thickness compared to uniform structural mass. Within respective groups, CBT-N12 outperforms CBT-N6 by approximately 7.9%, 14.3%, 14.3%, and 14.5% for CBTs with the same structural mass. In cases with equal thickness, varying N significantly influences SEA, with CBT-N12 surpassing CBT-N6 by around 35.7%, 42.5%, 42.4%, and 45.6% in corresponding groups. Dynamic loading positively impacts the energy absorption of CBTs. Increased impact velocities lead to elevated SEA and MCF, attributed to inertial effects. Impact velocity significantly influences the deformation pattern of CBTs, with higher velocities increasing the likelihood of mixed deformation modes. Moreover, a proper cross-section design can further enhance the SEA of original CBTs. A developed theoretical model

proficiently predicts mean crushing force, demonstrating robust agreement with numerical outcomes. The crashworthiness of CBTs surpasses that of typical competing multicell structures and recently developed biomimetic structures of the same mass. This emphasizes that CBTs offer an effective solution for developing lightweight, high-performance, energy-absorbing multicellular structures.

Acknowledgments

The supports of the National Natural Science Foundation of China (Grant No.11922206,12172125,12272132) and 111 Project (B16015) are acknowledged. Many thanks to Prof. James Mauseth of the University of Texas for granting permission to use Fig.1f.

Appendix A. The crushing performances of the typical energy absorbing structures

Table A1. The crushing performances of the typical energy absorbing structure with the same mass.

Type	Deformation mode	SEA(J/g)	CFE (%)	Type	Deformation mode	SEA(J/g)	CFE (%)
TST[59]		6.37	51	HBS[44]		9.65	56
QST-I[63]		7.48	56	BFMCT[69]		8.09	60
QST-II [63]		5.02	47	BHMBT[70]		8.92	67
FST[64]		6.44	52	BPS[71]		6.82	68

BHST[48]	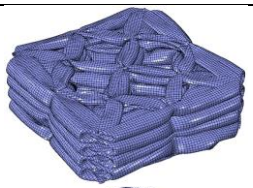	7.94	74	MHT[72]		6.84	55
MDST[65]		8.41	64	SHT[73]		5.12	47
ATST[66]	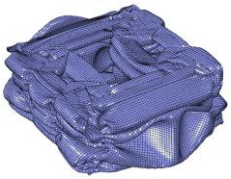	8.06	58	BHS[71]		6.5	63
TCT[67]		6.4	48	BHMHT[47]		7.92	77
QCT[67]		6.77	51	HMHT[74]		8.88	70
MBT[68]		8.06	61	SIMT[75]		7.22	62

References

[1] Yang W, Dong S, Zhu X, Ren S, Li L. Superior energy absorption performance of layered aux-hex honeycomb filled tubes. Int J Mech Sci 2022;234:107702. https://doi.org/10.1016/j.ijmecsci.2022.107702.

[2] Wang J, Liu Y, Wang K, Yao S, Peng Y, Rao Y, et al. Progressive collapse behaviors and mechanisms of 3D printed thin-walled composite structures under multi-conditional loading. Thin-Walled Struct 2022;171. https://doi.org/10.1016/j.tws.2021.108810.

[3] Wang J, Zhang Y, He N, Wang CH. Crashworthiness behavior of Koch fractal structures. Mater Des 2018;144:229–44. https://doi.org/10.1016/j.matdes.2018.02.035.

[4] Zhang D, Lu G, Ruan D, Fei Q. Energy absorption in the axial crushing of hierarchical circular tubes. Int J Mech Sci 2020;171:105403. https://doi.org/10.1016/j.ijmecsci.2019.105403.

[5] Li Q, Xiao Q, Liu X, Cheng X, Mao C, Hu H. Hierarchical double-hat beam for axial crashworthiness. Aerosp Sci Technol 2023;141:108515. https://doi.org/10.1016/j.ast.2023.108515.

[6] Alexander JM. An approximate analysis of the collapse of thin cylindrical shells under axial loading. Q J Mech Appl Math 1960;13:10–5. https://doi.org/10.1093/qjmam/13.1.10.

[7] Hsu SS, Jones N. Quasi-static and dynamic axial crushing of thin-walled circular stainless steel, mild steel and aluminium alloy tubes. Int J Crashworthiness 2004;9:195–217. https://doi.org/10.1533/ijcr.2004.0282.

[8] Guillow SR, Lu G, Grzebieta RH. Quasi-static axial compression of thin-walled circular aluminium tubes. Int J Mech Sci 2001;43:2103–23. https://doi.org/10.1016/S0020-7403(01)00031-5.

[9] Yang F, Fan H, Meguid SA. Effect of foam-filling on collapse mode transition of thin-walled circular columns under axial compression: Analytical, numerical and experimental studies. Int J Mech Sci 2019;150:665–76. https://doi.org/10.1016/j.ijmecsci.2018.10.047.

[10] Tian K, Zhang Y, Yang F, Zhao Q, Fan H. Enhancing energy absorption of circular tubes under oblique loads through introducing grooves of non-uniform depths. Int J Mech Sci 2020;166. https://doi.org/10.1016/j.ijmecsci.2019.105239.

[11] Fan Z, Lu G, Yu TX, Liu K. Axial crushing of triangular tubes. Int J Appl Mech 2013;5. https://doi.org/10.1142/S1758825113500087.

[12] Zhang XW, Su H, Yu TX. Energy absorption of an axially crushed square tube with a buckling initiator. Int J Impact Eng 2009;36:402–17. https://doi.org/10.1016/j.ijimpeng.2008.02.002.

[13] Xie S, Wang N. Crashworthiness analysis of multi-cell square tubes under axial loads. Int J Mech Sci 2017;121:106–18. https://doi.org/10.1016/j.ijmecsci.2016.12.005.

[14] Zhang Z, Liu N, Zhang Z, Xia X, Wang Z, Ding J, et al. Compression performances of composite aluminum foam tubes. Int J Mech Sci 2023;242:108039. https://doi.org/10.1016/j.ijmecsci.2022.108039.

[15] Zhang J, Guo H. Large deflection of rectangular sandwich tubes with metal foam core. Compos Struct 2022;293:115745. https://doi.org/10.1016/j.compstruct.2022.115745.

[16] Chen J, Li E, Liu W, Mao Y, Hou S. Sustainable composites with ultrahigh energy absorption from beverage cans and polyurethane foam. Compos Sci Technol 2023;239:110047. https://doi.org/10.1016/j.compscitech.2023.110047.

694 [17] Xie S, Zhang J, Liu X, Zheng S, Liu Z. A reinforced energy-absorbing structure formed by
695 combining multiple aluminum foam-filled open-hole tubes. Int J Mech Sci 2022;224:107319.
696 https://doi.org/10.1016/j.ijmecsci.2022.107319.
697 [18] Zhang J, Ye Y, Zhu Y, Yuan H, Qin Q, Wang T. On axial splitting and curling behaviour of circular
698 sandwich metal tubes with metal foam core. Int J Solids Struct 2020;202:111–25.
699 https://doi.org/10.1016/j.ijsolstr.2020.06.021.
700 [19] Zhang J, Guo H, Du J, Yuan H, Zhu Y, Qin Q. Splitting and curling collapse of metal foam core
701 square sandwich metal tubes: Experimental and theoretical investigations. Thin-Walled Struct
702 2021;169:108346. https://doi.org/10.1016/j.tws.2021.108346.
703 [20] Zhang J, Ye Y, Li J, Zhu Y, Yuan H, Qin Q, et al. Dynamic collapse of circular metal foam core
704 sandwich tubes in splitting and curling mode. Thin-Walled Struct 2021;161:107464.
705 https://doi.org/10.1016/j.tws.2021.107464.
706 [21] Pan J, Zhu W, Yang K, Hu L, Chen Y. Energy absorption of discretely assembled composite self-
707 locked systems. Compos Struct 2022;292:115686.
708 https://doi.org/10.1016/j.compstruct.2022.115686.
709 [22] Gao Q, Liao WH. Energy absorption of thin walled tube filled with gradient auxetic structures-
710 theory and simulation. Int J Mech Sci 2021;201:106475.
711 https://doi.org/10.1016/j.ijmecsci.2021.106475.
712 [23] Zhang Z jia, Huang L, Li B chao, Chen T, Zhang Q cheng, Jin F. Design of a novel multi-walled
713 tube-reinforced aluminum foam for energy absorption. Compos Struct 2021;276:114584.
714 https://doi.org/10.1016/j.compstruct.2021.114584.
715 [24] Chang B, Zheng Z, Zhang Y, Zhao K, He S, Yu J. Crashworthiness design of graded cellular
716 materials: An asymptotic solution considering loading rate sensitivity. Int J Impact Eng
717 2020;143:103611. https://doi.org/10.1016/j.ijimpeng.2020.103611.
718 [25] Fu X, Zhang X, Huang Z. Axial crushing of Nylon and Al/Nylon hybrid tubes by FDM 3D printing.
719 Compos Struct 2021;256:113055. https://doi.org/10.1016/j.compstruct.2020.113055.
720 [26] Wu J, Chen X, Zhu H, Wang P, Jin F, Fan H. Meta-honeycomb sandwich tubes: Designing,
721 manufacturing, and crashworthiness performance. Compos Sci Technol 2023;240:110096.
722 https://doi.org/10.1016/j.compscitech.2023.110096.

[27] Hu LL, Cai DY, Wu GP, He XL, Yu TX. Influence of internal pressure on the out-of-plane dynamic behavior of circular-celled honeycombs. Int J Impact Eng 2017;104:64–74. https://doi.org/10.1016/j.ijimpeng.2017.02.004.

[28] Hu LL, Zeng ZH, Yu TX. Axial crushing of pressurized cylindrical tubes. Int J Mech Sci 2016;107:126–35. https://doi.org/10.1016/j.ijmecsci.2016.01.011.

[29] Zhang XW, Yu TX. Energy absorption of pressurized thin-walled circular tubes under axial crushing. Int J Mech Sci 2009;51:335–49. https://doi.org/10.1016/j.ijmecsci.2009.03.002.

[30] Wang P, Yang F, Fan H, Lu G. Bio-inspired multi-cell tubular structures approaching ideal energy absorption performance. Mater Des 2023;225. https://doi.org/10.1016/j.matdes.2022.111495.

[31] Xu P, Guo W, Yang L, Yang C, Ruan D, Xu J, et al. Crashworthiness analysis of the biomimetic lotus root lattice structure. Int J Mech Sci 2023:108774. https://doi.org/10.1016/j.ijmecsci.2023.108774.

[32] Ha NS, Lu G, Xiang X. High energy absorption efficiency of thin-walled conical corrugation tubes mimicking coconut tree configuration. Int J Mech Sci 2018;148:409–21. https://doi.org/10.1016/j.ijmecsci.2018.08.041.

[33] Li Y, Hu D, Yang Z. Crashworthiness design of a sponge-inspired multicell tube under axial crushing. Int J Mech Sci 2023;244:108070. https://doi.org/10.1016/j.ijmecsci.2022.108070.

[34] Ma W, Li Z, Xie S. Crashworthiness analysis of thin-walled bio-inspired multi-cell corrugated tubes under quasi-static axial loading. Eng Struct 2020;204:110069. https://doi.org/10.1016/j.engstruct.2019.110069.

[35] Ma W, Xie S, Li Z. Mechanical performance of bio-inspired corrugated tubes with varying vertex configurations. Int J Mech Sci 2020;172:105399. https://doi.org/10.1016/j.ijmecsci.2019.105399.

[36] Liang H, Hao W, Sun H, Pu Y, Zhao Y, Ma F. On design of novel bionic bamboo tubes for multiple compression load cases. Int J Mech Sci 2022;218:107067. https://doi.org/10.1016/j.ijmecsci.2022.107067.

[37] Gong C, Bai Z, Wang Y, Zhang L. On the crashworthiness performance of novel hierarchical multi-cell tubes under axial loading. Int J Mech Sci 2021;206:106599. https://doi.org/10.1016/j.ijmecsci.2021.106599.

[38] Jin M, Hou X, Yin G, Yao R, Gao J, Deng Z. Improving the crashworthiness of bio-inspired multi-cell thin-walled tubes under axial loading: Experimental, numerical, and theoretical studies. Thin-Walled Struct 2022;177:109415. https://doi.org/10.1016/j.tws.2022.109415.

[39] Liu K, Yu Z, Wang K, Jing L. Crashworthiness of bamboo-inspired circular tubes used for the energy absorber of rail vehicles. Acta Mech Sin Xuebao 2022;38. https://doi.org/10.1007/s10409-022-22014-9.

[40] Chen BC, Zou M, Liu GM, Song JF, Wang HX. Experimental study on energy absorption of bionic tubes inspired by bamboo structures under axial crushing. Int J Impact Eng 2018;115:48–57. https://doi.org/10.1016/j.ijimpeng.2018.01.005.

[41] Palombini FL, Mariath JE de A, Oliveira BF de. Bionic design of thin-walled structure based on the geometry of the vascular bundles of bamboo. Thin-Walled Struct 2020;155:106936. https://doi.org/10.1016/j.tws.2020.106936.

[42] Hu D, Wang Y, Song B, Dang L, Zhang Z. Energy-absorption characteristics of a bionic honeycomb tubular nested structure inspired by bamboo under axial crushing. Compos Part B Eng 2019;162:21–32. https://doi.org/10.1016/j.compositesb.2018.10.095.

[43] Sethi A, Budarapu PR, Vusa VR. Nature-inspired bamboo-spiderweb hybrid cellular structures for impact applications. Compos Struct 2023;304:116298. https://doi.org/10.1016/j.compstruct.2022.116298.

[44] Xiao Y, Yin H, Fang H, Wen G. Crashworthiness design of horsetail-bionic thin-walled structures under axial dynamic loading. Int J Mech Mater Des 2016;12:563–76. https://doi.org/10.1007/s10999-016-9341-6.

[45] Yin H, Xiao Y, Wen G, Qing Q, Wu X. Crushing analysis and multi-objective optimization design for bionic thin-walled structure. Mater Des 2015;87:825–34. https://doi.org/10.1016/j.matdes.2015.08.095.

[46] Jin M, Hou X, Yin G, Yao R, Gao J, Deng Z. Improving the crashworthiness of bio-inspired multi-cell thin-walled tubes under axial loading: Experimental, numerical, and theoretical studies. Thin-Walled Struct 2022;177:109415. https://doi.org/10.1016/j.tws.2022.109415.

[47] Gao Z, Zhang H, Zhao J, Ruan D. The axial crushing performance of bio-inspired hierarchical multi-cell hexagonal tubes. Int J Mech Sci 2023;239:107880. https://doi.org/10.1016/j.ijmecsci.2022.107880.

[48] Ha NS, Pham TM, Hao H, Lu G. Energy absorption characteristics of bio-inspired hierarchical multi-cell square tubes under axial crushing. Int J Mech Sci 2021;201:106464. https://doi.org/10.1016/j.ijmecsci.2021.106464.

[49] Schwager H, Masselter T, Speck T, Neinhuis C. Functional morphology and biomechanics of branch-stem junctions in columnar cacti. Proc R Soc B Biol Sci 2013;280:20132244. https://doi.org/10.1098/rspb.2013.2244.

[50] Wang CY, Lu G, Zhao WZ, Wang Y. Modeling and multi-objective optimization of a bionic crash box with folding deformation. Struct Multidiscip Optim 2020;61:283–99. https://doi.org/10.1007/s00158-019-02360-1.

[51] Talley S, Iaccarino G, Mungal G, Mansour NN. An experimental and computational investigation of flow past cacti. Annu Res Briefs, Cent Turbul Res Ames/Stanford Univ 2001;0015:51–63. https://doi.org/https://api.semanticscholar.org/CorpusID:27972580.

[52] Malik FT, Clement RM, Gethin DT, Kiernan M, Goral T, Griffiths P, et al. Hierarchical structures of cactus spines that aid in the directional movement of dew droplets. Philos Trans R Soc A Math Phys Eng Sci 2016;374:20160110. https://doi.org/10.1098/rsta.2016.0110.

[53] Mastersviat. Cactus section. Https://WwwDreamstimeCom/Stock-Photo-Cactus-Section-Green-Shashed-Now-Image51454007,2022-09-12 n.d. https://www.dreamstime.com/mastersviat_info.

[54] James D. Mauseth. Modifications to the Cactus Cortex. Http://WwwSbsUtexasEdu/Mauseth/ResearchOnCacti/Cortex%20textHtm n.d. http://www.sbs.utexas.edu/mauseth/ResearchOnCacti/cortex text.htm.

[55] Chen J, Li E, Li Q, Hou S, Han X. Crashworthiness and optimization of novel concave thin-walled tubes. Compos Struct 2022;283:115109. https://doi.org/10.1016/j.compstruct.2021.115109.

[56] Santosa SP, Wierzbicki T, Hanssen AG, Langseth M. Experimental and numerical studies of foam-filled sections. Int J Impact Eng 2000;24:509–34. https://doi.org/10.1016/S0734-743X(99)00036-6.

[57] Xiang Y, Yu T, Yang L. Comparative analysis of energy absorption capacity of polygonal tubes, multi-cell tubes and honeycombs by utilizing key performance indicators. Mater Des 2016;89:689–96. https://doi.org/10.1016/j.matdes.2015.10.004.

[58] Xiang Y, Wang M, Yu T, Yang L. Key Performance Indicators of Tubes and Foam-Filled Tubes Used as Energy Absorbers. Int J Appl Mech 2015;7:1–20. https://doi.org/10.1142/S175882511550060X.

[59] Chen W, Wierzbicki T. Relative merits of single-cell, multi-cell and foam-filled thin-walled structures in energy absorption. Thin-Walled Struct 2001;39:287–306. https://doi.org/10.1016/S0263-8231(01)00006-4.

[60] Abramowicz W, Jones N. Dynamic progressive buckling of circular and square tubes. Int J Impact Eng 1986;4:243–70. https://doi.org/10.1016/0734-743X(86)90017-5.

[61] Zhang X, Zhang H. Theoretical and numerical investigation on the crush resistance of rhombic and kagome honeycombs. Compos Struct 2013;96:143–52. https://doi.org/10.1016/j.compstruct.2012.09.028.

[62] Zhang X, Zhang H. Numerical and theoretical studies on energy absorption of three-panel angle elements. Int J Impact Eng 2012;46:23–40. https://doi.org/10.1016/j.ijimpeng.2012.02.002.

[63] Tran TN, Hou S, Han X, Chau MQ. Crushing analysis and numerical optimization of angle element structures under axial impact loading. Compos Struct 2014;119:422–35. https://doi.org/10.1016/j.compstruct.2014.09.019.

[64] Zhang X, Zhang H. The crush resistance of four-panel angle elements. Int J Impact Eng 2015;78:81–97. https://doi.org/10.1016/j.ijimpeng.2014.12.004.

[65] Najafi A, Rais-Rohani M. Influence of cross-sectional geometry on crush characteristics of multi-cell prismatic columns. InCollection Tech. Pap. - AIAA/ASME/ASCE/AHS/ASC Struct. Struct. Dyn. Mater. Conf., 2008, p. 1–12. https://doi.org/10.2514/6.2008-2014.

[66] Li K, Zhang Y, Su L, Duan N, Shi W. Crushing mechanics of anti-tetrachiral column. Thin-Walled Struct 2022;175:109253. https://doi.org/10.1016/j.tws.2022.109253.

[67] Zhang X, Zhang H. Axial crushing of circular multi-cell columns. Int J Impact Eng 2014;65:110–25. https://doi.org/10.1016/j.ijimpeng.2013.12.002.

[68] Tang Z, Liu S, Zhang Z. Analysis of energy absorption characteristics of cylindrical multi-cell columns. Thin-Walled Struct 2013;62:75–84. https://doi.org/10.1016/j.tws.2012.05.019.

[69] Ha NS, Pham TM, Chen W, Hao H, Lu G. Crashworthiness analysis of bio-inspired fractal tree-like multi-cell circular tubes under axial crushing. Thin-Walled Struct 2021;169:108315. https://doi.org/10.1016/j.tws.2021.108315.

[70] Ha NS, Pham TM, Chen W, Hao H. Energy absorption characteristics of bio-inspired hierarchical multi-cell bi-tubular tubes. Int J Mech Sci 2023;251:108260. https://doi.org/10.1016/j.ijmecsci.2023.108260.

[71] Jiang B, Tan W, Bu X, Zhang L, Zhou C, Chou CC, et al. Numerical, theoretical, and experimental studies on the energy absorption of the thin-walled structures with bio-inspired constituent element. Int J Mech Sci 2019;164:105173. https://doi.org/10.1016/j.ijmecsci.2019.105173.

[72] Pirmohammad S, Marzdashti SE. Crushing behavior of new designed multi-cell members subjected to axial and oblique quasi-static loads. Thin-Walled Struct 2016;108:291–304. https://doi.org/10.1016/j.tws.2016.08.023.

[73] Zhang X, Zhang H. Energy absorption limit of plates in thin-walled structures under compression. Int J Impact Eng 2013;57:81–98. https://doi.org/10.1016/j.ijimpeng.2013.02.001.

[74] Gao Z, Xia F, Li J, Ruan D. Axial compression of multi-cell hexagonal tubes with novel hierarchical architectures: Numerical and theoretical analyses. Compos Struct 2023;318:117079. https://doi.org/10.1016/j.compstruct.2023.117079.

[75] He Y, Zhang X, Sun J, Shu X, Li X, Su B, et al. Energy absorption of self-similar inspired multi-cell hexagonal tubes. Eng Struct 2023;277:115455. https://doi.org/10.1016/j.engstruct.2022.115455.